The EDIBLES survey. VII. A survey of C2 and C3 in interstellar clouds

Haoyu Fan, Carlos M. R. Rocha, Martin Cordiner, Harold Linnartz, Nick L. J. Cox, Amin Farhang, Jonathan Smoker, Evelyne Roueff, Pascale Ehrenfreund, Farid Salama, et al.

A&A, 681, A6 (2024)
https://doi.org/10.1051/0004-6361/202243910

Astronomy & Astrophysics

The EDIBLES survey

VII. A survey of C_2 and C_3 in interstellar clouds

Haoyu Fan[1,2], Carlos M. R. Rocha[3], Martin Cordiner[4,5], Harold Linnartz[3], Nick L. J. Cox[6], Amin Farhang[7,8], Jonathan Smoker[9,10], Evelyne Roueff[11], Pascale Ehrenfreund[12], Farid Salama[13], Bernard H. Foing[14,12], Rosine Lallement[15], Heather MacIsaac[1,2], Klay Kulik[1,2], Peter Sarre[16], Jacco Th. van Loon[17], and Jan Cami[1,2,18]

[1] Department of Physics and Astronomy, The University of Western Ontario, London, ON N6A 3K7, Canada
e-mail: jcami@uwo.ca
[2] Institute for Earth and Space Exploration, The University of Western Ontario, London ON N6A 3K7, Canada
[3] Laboratory for Astrophysics, Leiden Observatory, Leiden University, PO Box 9513, 2300 RA Leiden, The Netherlands
[4] Astrochemistry Laboratory, NASA Goddard Space Flight Center, Code 691, 8800 Greenbelt Road, Greenbelt MD 20771, USA
[5] Department of Physics, The Catholic University of America, Washington DC 20064, USA
[6] Centre d'Études et de Recherche de Grasse, ACRI-ST, Av. Nicolas Copernic, 06130 Grasse, France
[7] School of Astronomy, Institute for Research in Fundamental Sciences, 19395-5531 Tehran, Iran
[8] Department of Physics, University of Tehran, North Karegar Ave., 14395-547 Tehran, Iran
[9] European Southern Observatory, Alonso de Cordova 3107, Casilla 19001, Vitacura, Santiago, Chile
[10] UK Astronomy Technology Centre, Royal Observatory, Blackford Hill, Edinburgh EH9 3HJ, UK
[11] LERMA, Observatoire de Paris, PSL Research University, CNRS, Sorbonne Universités, 92190 Meudon, France
[12] Leiden Observatory, Leiden University, PO Box 9513, 2300 RA Leiden, The Netherlands
[13] NASA Ames Research Centre, Space Science & Astrobiology Division, Moffett Field, California, USA
[14] ESTEC, ESA, Keplerlaan 1, 2201 AZ Noordwijk, The Netherlands
[15] GEPI, Observatoire de Paris, PSL Research University, CNRS, Université Paris-Diderot, Sorbonne Paris Cité, Place Jules Janssen, 92195 Meudon, France
[16] School of Chemistry, The University of Nottingham, University Park, Nottingham NG7 2RD, UK
[17] Lennard-Jones Laboratories, Keele University, ST5 5BG, UK
[18] SETI Institute, 339 Bernardo Ave., Suite 200, Mountain View CA, 94043, USA

Received 29 April 2022 / Accepted 21 August 2023

ABSTRACT

Context. Small linear carbon chain radicals such as C_2 and C_3 act as both the building blocks and dissociation fragments of larger carbonaceous species. Their rotational excitation traces the temperature and density of local environments. However, these homo-nuclear di- and triatomic species are only accessible through their electronic and vibrational features because they lack a permanent dipole moment, and high signal-to-noise ratio data are necessary as the result of their generally low abundances in the interstellar medium (ISM).

Aims. In order to improve our understanding of small carbonaceous species in the ISM, we carried out a sensitive survey of C_2 and C_3 using the ESO Diffuse Interstellar Bands Large Exploration Survey (EDIBLES) dataset. We also expanded our searches to C_4, C_5, and the $^{13}C^{12}C$ isotopologue in the most molecule-rich sightlines.

Methods. We fitted synthetic spectra generated following a physical excitation model to the C_2 (2-0) Phillips band to obtain the C_2 column density (N) as well as the kinetic temperature (T_{kin}) and number density (n) of the host cloud. The C_3 molecule was measured through its $\tilde{A} - \tilde{X}$ (000-000) electronic origin band system. We simulated the excitation of this band with a double-temperature Boltzmann distribution.

Results. We present the largest combined survey of C_2 and C_3 to date in which the individual transitions can be resolved. In total, we detected C_2 in 51 velocity components along 40 sightlines, and C_3 in 31 velocity components along 27 sightlines. Further analysis confirms the two molecules are detected in the same velocity components. We find a very good correlation between $N(C_2)$ and $N(C_3)$ with a Pearson correlation coefficient $r = 0.93$ and an average $N(C_2)/N(C_3)$ ratio of 15.5±1.4. A comparison with the behaviour of the C_2 diffuse interstellar bands (DIBs) shows that there are no clear differences among sightlines with and without detections of C_2 and C_3. This is in direct contrast to the better-studied non-C_2 DIBs, which have reduced strengths in molecule-rich environments, consistent with the idea that the C_2 DIBs are indeed a distinguishable DIB family. We also identify, for the first time, the $Q(2)$, $Q(3)$, and $Q(4)$ transitions of the $^{13}C^{12}C$ (2-0) Phillips band in the stacked average spectrum of molecule-rich sightlines, and estimate the isotopic ratio of carbon $^{12}C/^{13}C$ to be 79±8, consistent with literature results. At this stage it is not yet possible to identify these transitions in individual sightlines. Our search for the C_4 and C_5 optical bands was unsuccessful; even in stacked spectra no unambiguous identification could be made.

Key words. ISM: lines and bands – ISM: clouds – ISM: molecules

1. Introduction

Many carbon chain species have been detected via sub-millimetre and/or radio observations. However, due to the lack of a permanent dipole moment, bare carbon chains can only be accessed through their electronic and vibrational features. The simplest bare carbon molecule, interstellar C_2, was first detected towards the highly reddened star Cyg OB2 12 through its *A*-*X* (1-0) Phillips band in the near-IR (Souza & Lutz 1977). This was followed by more extensive observations of other bands and towards more targets (e.g. Hobbs & Campbell 1982; van Dishoeck & de Zeeuw 1984; Sonnentrucker et al. 2007; Wehres et al. 2010). The population on the C_2 rotational excitation ladder is determined simultaneously by collisional and radiative processes (van Dishoeck & Black 1982), which makes C_2 a powerful diagnostic tool for deriving local environmental factors, such as the kinetic temperature and density within the interstellar cloud.

An emission band around 4051 Å was first noted in the spectrum of comet Tebbutt (Huggins 1881), and Douglas (1951) subsequently assigned it to C_3. Observations of this band in diffuse interstellar environments have been difficult due to the much lower column density of C_3; the first tentative detection was made in 1995 in the highly reddened sightline towards HD 147889 (Haffner & Meyer 1995). C_3 molecules were also observed with *Herschel* in the ν_2 bending mode towards Sagittarius B2 and star-forming cores (Cernicharo et al. 2000; Mookerjea et al. 2010). To date, only a handful of measurements of the C_3 4051 Å band are available in the literature, and the data are mostly sightlines known to be molecule-rich (Maier et al. 2001; Roueff et al. 2002; Galazutdinov et al. 2002; Oka et al. 2003; Ádámkovics et al. 2003; Schmidt et al. 2014). In addition to the C_3 origin band, Schmidt et al. (2014) also reported electronic transitions involving vibrationally excited C_3 in its $\tilde{A}$ state. High-resolution spectra are required to accurately measure the C_3 column density. Once these measurements are available, individual transitions can be resolved, allowing the rotational excitation to be characterised, and the contribution from the higher *J*-levels to be determined (see e.g. Oka et al. 2003).

Small carbon molecules and chains are considered building blocks of more complex carbon-bearing compounds (Wakelam et al. 2009), and column density ratios of different carbon chains help us constrain the chemistry that drives their formation and destruction. The destruction process may also involve the photo-dissociation of (larger) polycyclic aromatic hydrocarbons (PAHs; Hrodmarsson et al. 2022). C_4 and C_5 molecules may be abundant in protoplanetary nebulae and circumstellar shells around evolved stars (Bernath et al. 1989; Cernicharo et al. 2002; Hargreaves et al. 2014), yet attempts to search for their spectral fingerprint in diffuse and translucent environments have been unsuccessful so far (Maier et al. 2002, 2004). Additionally, the isotopic ratio of carbon may trace Galactic chemical evolution (Milam et al. 2005). Hamano et al. (2019) report a marginal detection of the $Q(3)$ transition of the $^{13}C^{12}C$ (0,0) Phillips band towards Cyg OB2 12 (see also Gredel et al. 2001), and Giesen et al. (2020) reported the first detection of ^{13}CCC and $C^{13}CC$ through their ro-vibrational transitions at 1.9 THz. The measurement of an isotopologue also provides insight into local peculiarities since the isotope exchange rate that sets the isotopic fraction depends on environmental parameters such as temperature (see e.g. Rocha & Linnartz 2021; Visser et al. 2009).

Since their first discovery in the 1920s (Heger 1922), more than 500 diffuse interstellar bands (DIBs) have been identified in the near-UV, optical, and near-IR regions (Hobbs et al. 2008, 2009; Geballe et al. 2011; Fan et al. 2019). Despite this century-long history, the carriers of DIBs remain unknown, except for the five near-IR DIBs that were recently attributed to C_{60}^+ (Campbell et al. 2015; Walker et al. 2015; Cordiner et al. 2019; Ebenbichler et al. 2022). High-resolution observations reveal substructures within several DIBs that suggest they have molecular origins (Sarre et al. 1995; Kerr et al. 1998; Cami et al. 2004). Molecules of different types have been proposed as DIB carriers – from complex structures, such as (charged) fullerenes and PAHs (see e.g. Foing & Ehrenfreund 1994; Gredel et al. 2011; Salama et al. 2011; Salama & Ehrenfreund 2014, and their citations), to smaller molecules, such as carbon chains of different sizes (Motylewski et al. 2000; Oka et al. 2013; Zack & Maier 2014; see Herbig 1995 for a review) – despite the fact that none of their absorptions fully overlap with DIB features.

C_2 and C_3 molecules are present in the dense molecular regions of diffuse and translucent cloud environments. Their detection provides physical information on interstellar medium (ISM) environmental conditions, such as the kinetic temperature inferred from their rotational excitation. The column density ratios between C_2 and the 'first-generation molecules' H_2 and CH can trace the average ISM conditions of the sightline (Thorburn et al. 2003; Welty et al. 2013), similar to the use of the molecular hydrogen fraction, f_{H_2}, but presumably tracing deeper regions in the interstellar clouds (e.g. Fan et al. 2017). This information in turn can be compared to the behaviour of DIBs and provides constraints on their carriers (e.g. Cami et al. 1997; Sonnentrucker et al. 1997). This may eventually lead to the identification of the C_2 DIBs, whose equivalent widths become larger when the sightline is more abundant in C_2 (Thorburn et al. 2003).

In this paper we present a survey of C_2 and C_3 signals in the EDIBLES data. This dataset is briefly introduced in Sect. 2. We present our measuring methods and results for C_2 in Sect. 3 and for C_3 in Sect. 4. These results are discussed in Sect. 5, and we link these results to the behaviour of DIBs in Sect. 6. Section 7 describes our efforts to search for the $^{13}C^{12}C$, C_4, and C_5 transitions. We summarise our conclusions in Sect. 8.

2. Observations and spectral data

The ESO Diffuse Interstellar Bands Large Exploration Survey (EDIBLES) is a sensitive spectroscopic survey of a large sample of DIB sightlines towards early-type stars using the UV-visual echelle spectrograph (UVES; Dekker et al. 2000; Smoker et al. 2009) mounted on the Very Large Telescope (VLT). EDIBLES contains observations towards 123 sightlines with high spectral resolution ($R \sim 80\,000$ in the blue arm and ~100 000 in the red arm), high sensitivity (signal-to-noise ratio $S/N \sim 400$–1000 in the optical region), and covering a wide wavelength range (305–1042 nm). The program is described in Cox et al. (2017), and we also refer the reader to earlier publications that used EDIBLES data (i.e. Lallement et al. 2018; Elyajouri et al. 2018; Bacalla et al. 2019; MacIsaac et al. 2022) for more details.

In this paper, we focus on the C_2 (2-0) Phillips system around 8757 Å, and the C_3 $\tilde{A} - \tilde{X}$ origin band around 4051 Å. All spectra used in this work were obtained with the 437+860 setting of UVES. For sightlines with multiple observations, we interpolated, normalised, and co-added all available data into a single and high-quality spectrum for the final analysis.

3. C_2 models and measurements

Most studies target transitions from the C_2 $A^1\Pi_u \leftarrow X^1\Sigma_g^+$ Phillips system, especially the (1-0) band at 10 144 Å, the

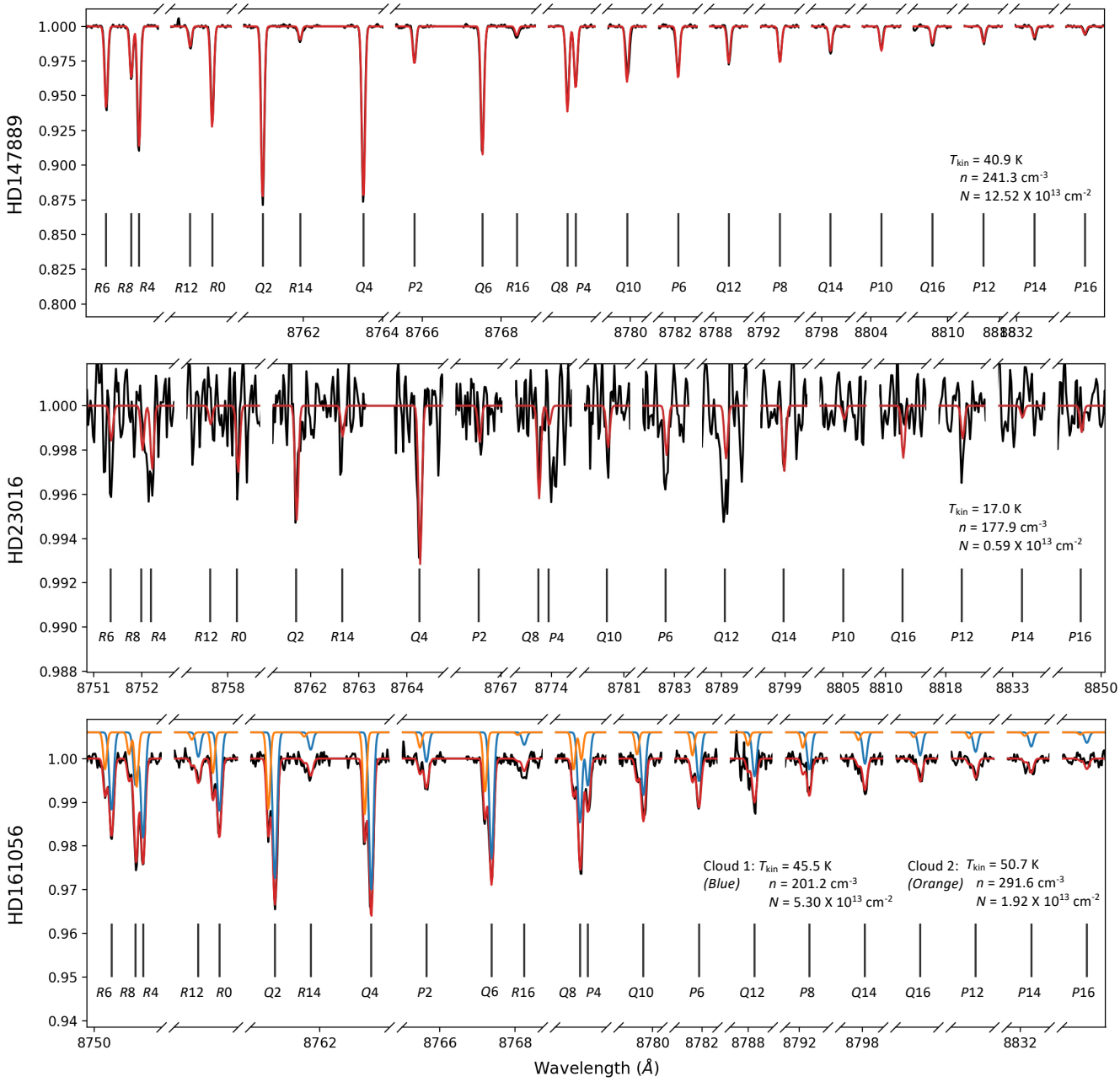

Fig. 1. Spectral segments from three representative sightlines for the C_2 (A-X) Phillips (2-0) band. HD 147889 (top) has the highest C_2 column density in our data sample. HD 23016 (middle) shows a tentative detection, as the strongest $Q(4)$ line is still below the 3σ detection limit. We considered multiple rotational lines simultaneously when deciding about possible identifications. The C_2 molecules are detected in two velocity components in HD 161056 (bottom). The combined model (red) is plotted against the spectral data, while synthetic spectra for the two velocity components (blue and orange) are plotted separately with an offset. We focus on the spectral segments around the C_2 transitions, and the wavelength grid is hence discrete. Rotational lines being considered in each sightline may differ due to telluric interference and/or data quality. These rotational lines are labelled with vertical bars. The best-fit parameters for the kinetic temperature, T_{kin}, number density, n, and the column density of the velocity component, N, are listed in each panel.

(2-0) band at 8757 Å, and the (3-0) band at 7719 Å (Souza & Lutz 1977; Hobbs & Campbell 1982; van Dishoeck & de Zeeuw 1984; van Dishoeck & Black 1986; Federman et al. 1994; Gredel 1999; Casu & Cecchi-Pestellini 2012). Even though the EDIBLES data cover both the (2-0) and (3-0) bands, we only used the former, which is stronger and less affected by telluric lines. Figure 1 shows spectral segments around the target transitions of the C_2 (2-0) band and the fitted model of three representative sightlines.

3.1. Line list and modelling of the C_2 (2-0) Phillips band

We adopted the wavelengths and oscillator strengths (f_{jj} values) of the C_2 (2-0) Phillips band from Sonnentrucker et al. (2007) for J up to 16 (Table 1). The $R(2)$ and $R(10)$ transitions at 8753.949 and 8753.578 Å were excluded due to a nearby CCD artefact.

van Dishoeck & Black (1982) provided a comprehensive model of the rotational excitation of C_2 by considering both radiative and collisional processes. The relative population of C_2 for different J-levels probes the kinetic temperature T_{kin} as

Table 1. Line list for the C_2 (2-0) Phillips bands.

Transition	λ_{jj} [(a)] (Å)	f_{jj} ($\times 10^4$)	Transition	λ_{jj} [(a)] (Å)	f_{jj} ($\times 10^4$)
$R(6)$	8750.848	4.31	$Q(8)$	8773.221	7.00
$R(8)$	8751.486	4.12	$P(4)$	8773.430	2.34
$R(4)$	8751.685	4.66	$Q(10)$	8780.141	7.00
$R(10)$ [(b)]	8753.578	4.00	$P(6)$	8782.308	2.69
$R(2)$ [(b)]	8753.949	5.60	$Q(12)$	8788.558	7.00
$R(12)$	8757.127	3.92	$P(8)$	8792.648	2.88
$R(0)$	8757.686	14.00	$Q(14)$	8798.459	7.00
$Q(2)$	8761.194	7.00	$P(10)$	8804.499	3.00
$R(14)$	8762.145	3.86	$Q(16)$	8809.841	7.00
$Q(4)$	8763.751	7.00	$P(12)$	8817.826	3.08
$P(2)$	8766.031	1.40	$P(14)$	8832.679	3.14
$Q(6)$	8767.759	7.00	$P(16)$	8849.071	3.18
$R(16)$	8768.627	3.82			

Notes. Data are taken from Sonnentrucker et al. (2007). [(a)]Air wavelength. [(b)]Not included in the measurements due to adjacent CCD artefact.

well as the number density n. Snow & McCall (2006) turned this model into an online C_2 Calculator[1] that computes the relative population for different J-levels at given the kinematic temperature $T_{\rm kin}$ and the H + H_2 number density n. We generated a finely sampled grid from this calculator, for $T_{\rm kin}$ between 10 and 100 K with an interval of 1 K, and n between 10 and 1000 cm^{-3} with an interval of 10 cm^{-3}. The parameter grid is then interpolated using a 2D cubic spline.

We followed the routine described in Elyajouri et al. (2018) to generate synthetic C_2 spectra and assumed Gaussian optical depth profiles for all C_2 transitions (see also Kokkin et al. 2007). With the knowledge on the relative population on different J-levels, the total column density N, the Gaussian broadening parameter b, and the velocity offset $v_{\rm off}$ (relative to the barycentric frame), we were then able to calculate the opacity spectrum for a velocity component. For each of the sightlines, opacity spectra for all velocity components where C_2 transitions can be discerned are co-added and then converted to flux units. This synthetic spectrum was finally convolved with a Gaussian kernel with a full width at half maximum (FWHM) of 2.8 km s^{-1} that simulates the instrumental profile.

3.2. C_2 measurements and results

Under typical ISM conditions, the $Q(2)$, $Q(4)$, and $Q(6)$ are the strongest transitions of the C_2 (A-X) band. We first visually examined the presence of these absorption lines to screen the target sightlines for a more detailed model-fitting process. We paid close attention to the asymmetries and multiple peaks in the line profiles and compared them to the velocity components identified in the Na I 3302 Å doublet. Such efforts helped us determine whether the C_2 lines should be measured in multiple velocity components, each of which is characterised by its own set of parameters (i.e. the kinetic temperature $T_{\rm kin}$, the number density n, the total column density N, the broadening factor b, and the velocity offset $v_{\rm off}$ relative to the barycentric frame).

The rotational transitions of the C_2 (2-0) Phillips band span a ~100 Å wavelength range. Since they take up a very limited fraction of the window, we chose to focus on spectral segments with the target C_2 transitions without having to fit a global continuum. These segments are 1.8 Å or ~60 km s^{-1} on each side of the target lines, and are combined when a segment overlaps with another. We normalised these segments with third-order polynomial continua. Telluric lines were identified from the HITRAN database (Rothman 2021) in this process. In most cases, the telluric lines could be corrected by fitting them with a Gaussian profile so their presence would not affect the normalisation. If that was not possible, the spectral segment was excluded from the fitting process.

The synthetic spectrum was fitted to the normalised data using a customised Python script based on the Sherpa package (Freeman et al. 2001). The parameters in the model were optimised using a Levenberg-Marquardt χ^2 minimisation. The 1σ errors were estimated by independently tuning each parameter from its optimal value until the sum of χ^2 reached $\chi^2_{\rm min} + 1$.

The C_2 (2-0) Phillips band is detected at the 3σ level in 37 sightlines, and tentatively in another 3 sightlines[2] Nine of these sightlines – HD 41117, HD 61827, HD 112272, HD 147084, HD 149404, HD 161056, HD 183143, HD 186745, and HD 186841 – contain two velocity components in which the target C_2 band is detected, while three components are detected towards HD 167971. Figure 1 demonstrates spectral data and best-fit results of three representative sightlines and Appendix A contains a gallery of all 40 sightlines. The fitted parameters and their 1σ uncertainties are tabulated in Table C.1. In the table we also include literature values for targets that have been studied previously. For the sightlines in common with our study, both the kinetic temperatures and densities we derive are in good agreement with existing literature values, and typically with smaller uncertainties.

3.3. Temperatures and densities of C_2-bearing clouds

We supplemented our derived values for $T_{\rm kin}$ and n in 40 sightlines with literature values for an additional 36 targets (see the bottom part of Table C.1) to study the distribution function of these parameters.

Figure 2 shows the distribution of the derived kinetic temperatures and densities using results from our study (red) as well as including literature values (blue). The temperature distribution peaks in the 30–40 K range, with an unweighted average kinetic temperature (using all values) of 40±16 K; we also note that the median value is 40 K. Only four values are higher than 60 K. The density distribution is similarly strongly peaked in the 100–200 cm^{-3} range. The unweighted average and standard deviation is 247 ±146 cm^{-3}, but the median value is 202.8 cm^{-3} and only six values are above 500 cm^{-3}. As can be ascertained from Table C.1, these values typically have large uncertainties.

4. C_3 models and measurements

The strongest C_3 transitions in the optical region lie around 4051 Å and are from the origin 000-000 band of the $\tilde{A}^1\Pi_u - \tilde{X}^1\Sigma_g^+$ system. This band is characterised by a piled-up Q-branch in the centre, while the rotational lines from the P- and R-branches can be resolved in our data (Fig. 3). This allows us to determine the rotational excitation and thus the total column density

[1] http://dib.uiuc.edu/c2/

[2] We use the term 'tentative detection' when no individual transition reaches the 3σ detection limit set by the S/N. In such cases, we are still able to extract some information by simultaneously fitting the entire band, albeit with decreased accuracy.

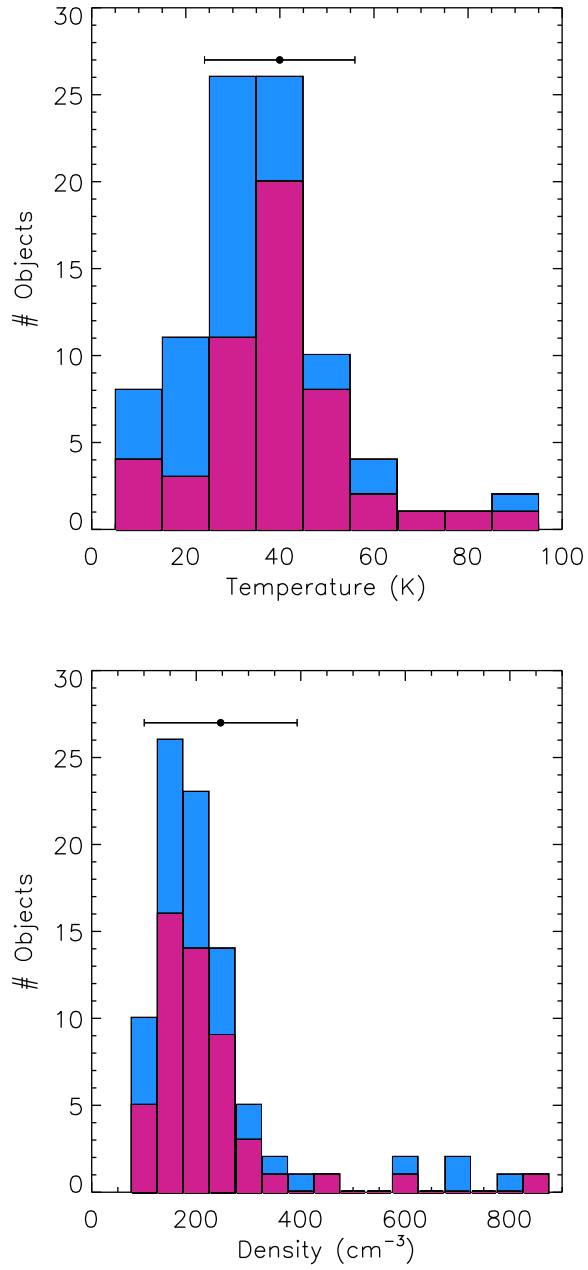

Fig. 2. Histograms of the kinetic temperatures (top) and densities (bottom) in C_2-bearing clouds. In both panels, the red histogram represents the values determined in this study; the blue histogram also includes literature values (see Table C.1). The single data point with an error bar indicates the (unweighted) average of all values and the standard deviation.

of C_3 in a more accurate way by including the contributions from the higher J-levels whose transitions are too weak to be detected. Some transitions involving vibrationally excited levels in the upper $\tilde{A}$ state have recently been detected in diffuse interstellar environments (Schmidt et al. 2014). These transitions are also within the EDIBLES wavelength range, but in wavelength ranges where we lack sufficient S/N to detect these weak lines.

4.1. Line list of the C_3 $\tilde{A} - \tilde{X}$ band

Wavelengths of the C_3 $\tilde{A} - \tilde{X}$ origin band transitions are reported in several works (e.g. Gausset et al. 1965; McCall et al. 2003; Tanabashi et al. 2005; Martin-Drumel et al. 2023).

Table 2. Line list used to simulate the C_3 $\tilde{A} - \tilde{X}$ 000-000 band.

Rotational line	λ_{jj} (Å)	f_{jj} ($\times 10^3$)	Rotational line	λ_{jj} (Å)	f_{jj} ($\times 10^3$)
$R(20)^{(a)}$	4049.808	4.29	$Q(12)$	4051.918	7.97
$R(18)^{(a)}$	4049.861	4.32	$P(4)$	4052.054	1.57
$R(16)^{(a)}$	4049.962	4.36	$Q(14)$	4052.077	7.98
$R(14)$	4050.075	3.49	$Q(6)^{(b)}$	4052.122	0.28
$R(12)$	4050.191	3.58	$P(4)^{(b)}$	4052.180	0.86
$R(10)$	4050.327	3.73	$Q(16)$	4052.257	7.98
$R(6)^{(b)}$	4050.401	0.58	$P(6)$	4052.412	2.56
$R(8)$	4050.484	3.95	$Q(18)$	4052.459	7.99
$R(4)^{(b)}$	4050.567	0.49	$P(8)^{(b)}$	4052.521	0.39
$R(6)$	4050.661	4.21	$Q(20)$	4052.683	7.99
$Q(2)^{(b)}$	4050.746	0.45	$P(8)$	4052.782	2.82
$R(4)$	4050.857	4.44	$Q(22)^{(a)}$	4052.938	7.99
$R(2)$	4051.055	3.78	$P(10)$	4053.169	2.87
$R(2)^{(b)}$	4051.190	2.08	$Q(24)^{(a)}$	4053.201	7.99
$R(0)$	4051.255	4.22	$Q(26)$	4053.479	7.99
$R(0)^{(b)}$	4051.396	10.58	$P(12)$	4053.577	2.87
$Q(2)$	4051.448	6.87	$Q(28)$	4053.783	8.00
$Q(4)$	4051.506	7.70	$P(14)$	4054.005	2.86
$Q(6)$	4051.578	7.89	$Q(30)^{(a)}$	4054.108	8.00
$Q(8)^{(a)}$	4051.670	7.95	$P(16)^{(a)}$	4054.447	3.64
$Q(10)$	4051.782	7.96	$P(18)^{(a)}$	4054.902	3.68
$P(2)$	4051.820	1.06	$P(20)^{(a)}$	4055.369	3.71

Notes. The wavelengths and f_{jj} values are taken from Schmidt et al. (2014) unless otherwise specified. $^{(a)}$Wavelengths adopted from Tanabashi et al. (2005) and f_{jj} values based on theoretical calculations. $^{(b)}$Perturbed transition.

Zhang et al. (2005) report the presence of at least two perturbing energy levels that are close to the upper $\tilde{A}\ ^1\Pi_u$ state. These perturbing states would change the observation in two ways, where a) the effective f_{jj} values of the original transitions are smaller than theoretically predicted, and b) some of these perturbed lines are strong enough to be detected in the spectrum. Such interference, especially when the lower J-levels are involved, should be considered when simulating the C_3 spectrum (Schmidt et al. 2014; Haddad et al. 2014).

Table 2 lists the 44 transitions we considered to simulate the C_3 4051 Å band, including the original Q-branch lines for J up to 30, the original P- and R-branch lines for J up to 20, and eight strong perturbed lines reported in Schmidt et al. (2014). The wavelengths of the target transitions are adopted from Table 3 of Schmidt et al. (2014). For the rotational lines that are not included in that source, we used the values from Tanabashi et al. (2005) after removing their correction of 0.04 cm^{-1} on the wavenumbers. This treatment provides better agreement on the lower J-level transitions between Tanabashi et al. (2005) and Schmidt et al. (2014; as well as Gausset et al. 1965 and McCall et al. 2003).

We adopted the more widely used oscillator strength of the C_3 000-000 band as $f_{000} = 0.016$ (e.g. Maier et al. 2001; Ádámkovics et al. 2003; Oka et al. 2003; Schmidt et al. 2014). However, a slightly smaller value of $f_{000} = 0.0146$ is used in some studies (e.g. Roueff et al. 2002; Galazutdinov et al. 2002) due to the uncertainties in the Frank-Condon factor (see e.g. Perić-Radić et al. 1977; Jungen & Merer 1980). The C_3 column densities would be 10% larger if this smaller f_{000} value is

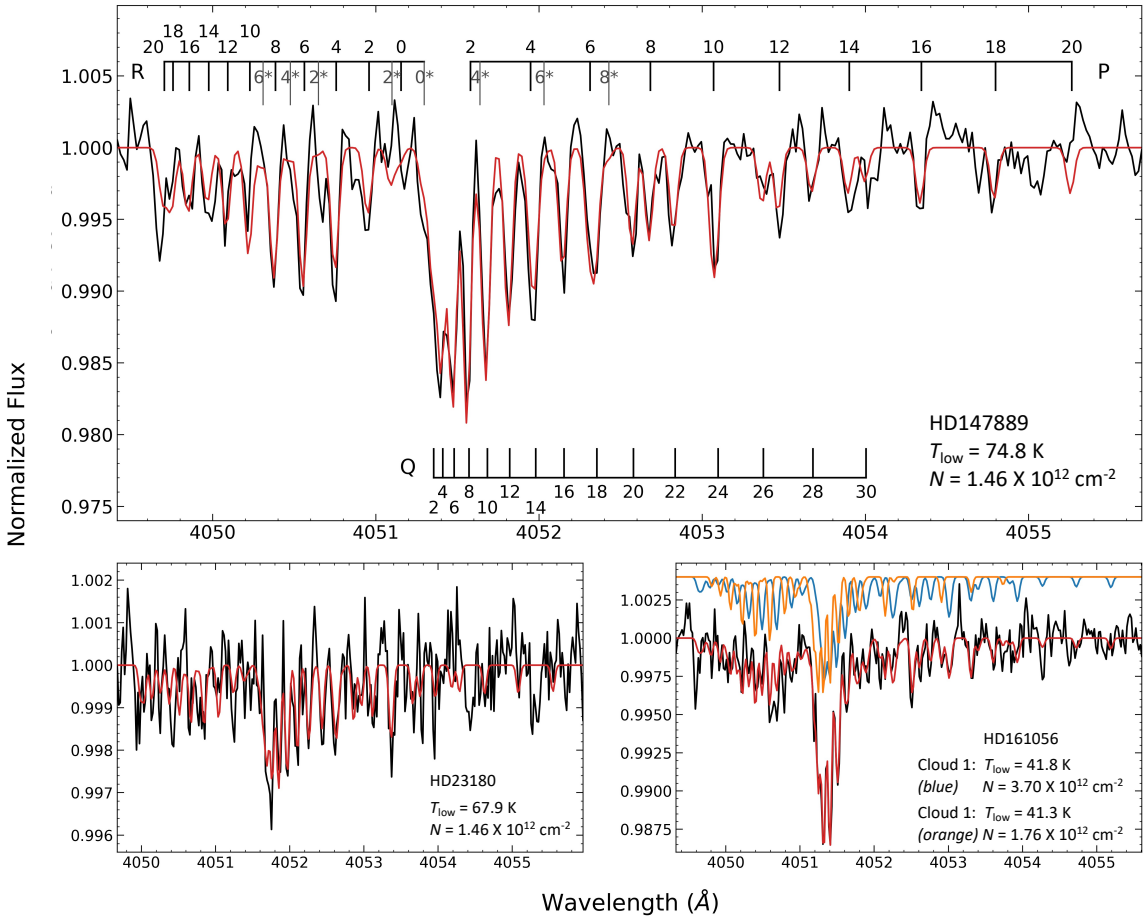

Fig. 3. C_3 $\tilde{A}^1\Pi_u - \tilde{X}^1\Sigma_g^+$ 000-000 band in three representative sightlines. Top panel: HD 147889, in addition to harbouring the largest $N(C_2)$, also harbours the largest $N(C_3)$ in our data sample. The transitions are all labelled, including those to the original and the perturbed upper energy levels (the latter are highlighted with asterisks; refer also to Sect. 4.1 and Table 2). Bottom panels: The C_3 band is tentatively detected towards HD 23180, mainly through its piled-up Q branch in the middle. The sightline of HD 161056 contains two velocity components of C_3. The synthetic spectra for the two components are plotted with a positive offset in different colours.

used. Without the perturbed lines, the f_{jj} values of the original transitions can be calculated as

$$f_{jj} = \begin{cases} f_{000} \times \dfrac{J+2}{2(2J+1)} & R\text{-branch} \\ f_{000} \times \dfrac{1}{2} & Q\text{-branch} \\ f_{000} \times \dfrac{J-1}{2(2J+1)} & P\text{-branch.} \end{cases} \quad (1)$$

Due to the presence of perturbed lines, the effective f_{jj} values are different from the theoretical calculations. We used the experimentally determined f_{jj} values from Schmidt et al. (2014), except for transitions not listed there. In that case, we used the theoretical results of Eq. (1). These transitions are mostly from the higher J-levels with limited population, and the interference from the perturbed lines becomes very subtle.

4.2. Excitation and modelling of C_3

Under typical diffuse interstellar conditions, C_3 molecules have a relatively short lifetime, and collisional processes may not significantly change the population of the higher J-levels (Roueff et al. 2002; Schmidt et al. 2014). Observations suggest that the rotational excitation of C_3 is characterised by two temperatures with the transition point around $J = 14$. The excitation temperature of lower J-levels, T_{low}, is governed more by collisions and is typically a few tens of kelvin, whilst the temperature for the higher J-levels, T_{high}, is governed more by radiative processes and is usually a few hundred kelvin (see e.g. Ádámkovics et al. 2003; Maier et al. 2001; Welty et al. 2013). The much higher excitation for the higher J-levels leads to a shallow decrease in their population, and in total the $J > 14$ levels may contribute ~15% of the total column density (Ádámkovics et al. 2003).

To simulate the rotational excitation of the C_3 molecules and obtain the relative population of different J-levels, we composed a two-temperature Boltzmann distribution model with the following steps:

1. Take the $J = 14$ population as reference, by defining $N(J = 14) = 1.0$.
2. Calculate the relative population of the lower J-levels $\{N_{low}\}$ from the Boltzmann distribution of temperature T_{low}: $\{N_{low}\} = \{N_{low}(J = 0), N_{low}(J = 2), N_{low}(J = 4), ..., N_{low}(J = 12), N(J = 14)\}$.
3. Similarly, calculate the relative population of higher J-levels (for J up to 100), $\{N_{high}\} = \{N(J = 14), N_{high}(J = 16), ..., N_{high}(J = 100)\}$, from the Boltzmann distribution of temperature T_{high}.
4. Combine $\{N_{low}\}$ and $\{N_{high}\}$ into $\{N_J\}$, where $\{N\} = \{N_{low}(J = 0), N_{low}(J = 2), ..., N_{low}(J = 12), N(J = 14), N_{high}(J = 16), ..., N_{high}(J = 100)\}$.

5. Scale $\{N_J\}$ so it adds up to unity.

Despite the approximation, this model provides results that agree well with the literature (see the next subsection). The rotational energies of the different J-levels required in the Boltzmann distribution are calculated using the molecular constants in Tanabashi et al. (2005) as follows:

$$\begin{aligned} E_J &= B \times J(J+1) - D \times [J(J+1)]^2 + H \times [J(J+1)]^3 \\ B &= 0.4305883\ \mathrm{cm}^{-1} \\ D &= 1.437 \times 10^{-6}\ \mathrm{cm}^{-1} \\ H &= 1.129 \times 10^{-10}\ \mathrm{cm}^{-1}. \end{aligned} \quad (2)$$

The column density of C_3 is typically one order of magnitude lower than C_2 and for the much weaker C_3 absorption strengths optically thin conditions can be assumed (Fig. 3). Becker et al. (1979) report the radiative lifetime of C_3 as approximately 200 ns, and natural broadening can hence be ignored. We thus used simple Gaussian profiles in flux units to simulate the rotational lines of the C_3 4051 Å band, and rotational lines from the same velocity component would share the same FWHM and velocity offset ($v_{\rm off}$, relative to barycentric frame) parameters. We also set a lower boundary of 3.0 km s^{-1} for the FWHM, so the Gaussian profiles have at least the instrumental width, in addition to physical processes that broaden the C_3 transitions.

4.3. Measurements and results

As for C_2, we first visually examined the target C_3 transitions, especially the more strongly piled-up Q branch contour. The C_3 $\tilde{A} - \tilde{X}$ 000-000 band spans a narrow wavelength window of ∼6 Å, and we used a cubic spline continuum to normalise the entire wavelength region. The compact distribution of the transitions hampers the identification of possible extra velocity components. We thus referred to the C_2 measurements and the Na I 3302 Å doublet of the same sightline to determine the number of components needed for the model. Each of these components is characterised by its own set of $T_{\rm low}$, $T_{\rm high}$, column density N, Gaussian width factor FWHM, and $v_{\rm off}$, which is relative to the barycentric frame. We followed the same routine as C_2 for parameter optimisation and error estimation (see Sect. 3.2).

The target C_3 band is detected at the 3σ level in 19 sightlines, and tentatively in another 8 sightlines[3]. These include 4 sightlines where C_3 is measured in two velocity components (HD 61827, HD 149404, HD 161056, and HD 186841). In Table 3 we summarise the C_3 measurements and compare to available literature values, and we find good agreement in most of the cases, especially with results from high-resolution data. The C_2 and C_3 detection are clearly linked; all sightlines with a C_3 detection (Table 3) also exhibit C_2 absorption. The best-fit models are visualised for three representative targets in Fig. 3 and the full gallery is available in Appendix B.

The temperature parameters may be less well determined when $N(C_3)$ is small, especially for $T_{\rm high}$. Assuming average excitation conditions where $T_{\rm low}$ = 50 K and $T_{\rm high}$ = 250 K, the higher J levels harbour ∼25% of the total population. This leaves less than 5% of the total equivalent width for each of the J-levels considered in our model, which is further divided into the P, Q, and R transitions. These transitions are then very weak and provide limited constraints on minimising the χ^2 during the fitting process.

[3] We use the term 'tentative detection' when the deepest point of the synthetic spectrum is shallower than 3σ from the continuum level.

5. C_2 versus C_3

In this section we compare the velocity offsets and column densities of C_2 and C_3 obtained in our survey (Fig. 4). Since there may be multiple velocity components in some sightlines, each data point in the plot represents an individual ISM cloud. We find the velocity offsets of C_2 and C_3 agree with each other (within uncertainties), which suggests the two molecules are detected in the same velocity components, and validates further comparison of their column densities.

The column densities of C_2 and C_3 show a tight correlation among the 30 velocity components from 26 sightlines with r = 0.93 (Fig. 4, lower panel). We find the best-fit line to have a relatively small intercept. The slope of the best-fit line, indicating the $N(C_2)/N(C_3)$ ratio, is 15.5±1.4. While it is widely agreed that $N(C_3)$ should be one magnitude lower than $N(C_2)$, it used to be difficult to determine the $N(C_2)/N(C_3)$ ratio with good accuracy due to the required high quality data. In a pioneering survey by Oka et al. (2003), the authors also found a good correlation between $N(C_2)$ and $N(C_3)$, and estimated a $N(C_2)/N(C_3)$ ratio of ∼40. However, since the individual rotational lines could not be resolved in their medium resolution data ($R \sim 38\,000$), Oka et al. (2003) focused on the piled-up Q branch and assumed it contributed half of the total intensity of the band. This approximation may underestimate contributions from the higher J-levels and hence $N(C_3)$ (Ádámkovics et al. 2003).

The $N(C_2)/N(C_3)$ ratio of 15.5 in this work is slightly larger than the value of ∼10 reported by Schmidt et al. (2014), and is in fact close to the prediction for a typical diffuse interstellar cloud with A_V ∼2.0 mag in the model presented by Schmidt et al. (2014). This is approximately the extinction of our targets (Cox et al. 2017). However, the $N(C_2)/N(C_3)$ ratio can be quite different in circumstellar environments, presumably related to the much higher density and/or enhanced radiation field. For example, literature reports column densities of both C_2 and C_3 to be $\sim 10^{15}$cm^{-2} towards the well-studied carbon star IRC+10216 (see e.g. Hinkle et al. 1988; Bakker et al. 1997; Cernicharo et al. 2000; Hargreaves et al. 2014), and $N(C_2)/N(C_3)$ ∼1.

In diffuse and translucent clouds the C_2 molecules may be formed bottom-up along the reaction $C^+ + CH \rightarrow C_2^+ + H$. The product then turns into C_2 molecules via multiple channels that consist of series of abstractions of H atoms and dissociative recombinations (e.g. Federman & Huntress 1989; Federman et al. 1994; Sonnentrucker et al. 2007). Oka et al. (2003) suggested that C_3 molecules are formed via dissociative recombination of C_3H^+ (Oka et al. 2003), while Bergeat & Loison (2001) advocate for non-negligible contribution from neutral-neutral reactions between C and C_2H_2. It is also possible for the two molecules to be formed from detachment of larger molecules in a top-down manner. In either case, there must be a strong chemical link between C_2 and C_3 since their column densities are tightly correlated.

6. C_2, DIBs, and C_2 DIBs

Thorburn et al. (2003) introduced the C_2 DIBs as 'a class of weak, narrow bands whose normalised equivalent widths $W(X)/W(6196)$ are well correlated, specifically with $N(C_2)/E_{B-V}$ via power laws'. The C_2 DIBs demonstrate different behaviour compared to the 'regular' non-C_2 DIBs, in particular in dense environments (see e.g. Fan et al. 2017). Contrary to their name, the C_2 DIBs may correlate better with E_{B-V} than with $N(C_2)$ (Elyajouri et al. 2018). The strong C_2 DIBs $\lambda\lambda$4963 and 4984 are detected in sightlines exposed to intense radiation fields and

Table 3. Best-fit parameters of the C_3 models in 27 sightlines.

Sightline [a]	This work [b]					Literature [c]		
	T_{low} (K)	T_{high} (K)	N (10^{12} cm^{-2})	$FWHM$ (km s^{-1})	v_{off} (km s^{-1})	T (K)	N (10^{12} cm^{-2})	Source
HD 23180 [d]	$74.8^{+12.0}_{-8.8}$	$275.5^{+60.2}_{-49.3}$	$1.46^{+0.12}_{-0.12}$	$4.47^{+0.49}_{-0.42}$	$13.2^{+1.2}_{-1.2}$	127.3 ± 3.9	1.27 ± 0.13	A03
HD 24398 [d]	$145.3^{+105.5}_{-41.5}$	$137.4^{+45.0}_{-34.3}$	$1.37^{+0.15}_{-0.15}$	$4.22^{+0.64}_{-0.52}$	$13.2^{+1.3}_{-1.3}$	132.0 ± 10.3	1.30 ± 0.35	A03
							1.00	O03
						50.0	1.37	R02
							1.00	M01
HD 27778	$49.2^{+3.5}_{-3.1}$	$253.1^{+55.8}_{-49.0}$	$2.79^{+0.16}_{-0.16}$	$5.56^{+0.61}_{-0.49}$	$14.7^{+1.3}_{-1.3}$		1.20 ± 0.30	O03
HD 45314	$59.5^{+6.5}_{-5.4}$	$143.7^{+39.4}_{-33.7}$	$1.80^{+0.12}_{-0.12}$	$4.66^{+0.45}_{-0.38}$	$17.0^{+1.2}_{-1.2}$			
HD 61827 (Comp.1)	$36.3^{+2.7}_{-2.5}$	$179.4^{+71.5}_{-60.7}$	$2.47^{+0.12}_{-0.12}$	$3.91^{+0.28}_{-0.24}$	$41.1^{+1.1}_{-1.1}$			
HD 61827 (Comp.2)	$54.6^{+6.4}_{-5.2}$	$196.7^{+56.8}_{-46.5}$	$1.83^{+0.14}_{-0.14}$	$3.11^{+0.31}_{-0.26}$	$34.5^{+1.1}_{-1.1}$			
HD 63804	$54.9^{+5.9}_{-4.8}$	$283.2^{+68.4}_{-57.4}$	$4.56^{+0.34}_{-0.34}$	$5.60^{+0.73}_{-0.57}$	$38.6^{+1.3}_{-1.4}$			
HD 73882 [d]	$30.0^{+1.2}_{-1.1}$	$286.7^{+77.3}_{-70.1}$	$3.34^{+0.10}_{-0.10}$	$3.58^{+0.12}_{-0.12}$	$20.4^{+1.0}_{-1.0}$			
HD 80558 [d]	$40.3^{+4.8}_{-3.7}$	1000.0	$1.68^{+0.24}_{-0.24}$	$6.48^{+1.46}_{-0.92}$	$19.6^{+2.2}_{-2.1}$			
HD 144217 [d]	$15.1^{+6.2}_{-4.1}$	100.0	$0.36^{+0.09}_{-0.08}$	$3.46^{+1.93}_{-0.85}$	$-10.5^{+1.7}_{-1.6}$		<0.38	G02
HD 147683	$87.4^{+19.8}_{-13.6}$	$115.0^{+30.4}_{-25.2}$	$1.64^{+0.12}_{-0.12}$	$3.98^{+0.40}_{-0.33}$	$-2.2^{+1.2}_{-1.2}$			
HD 147888	$58.1^{+6.4}_{-5.3}$	$167.0^{+46.1}_{-39.7}$	$1.35^{+0.09}_{-0.09}$	$3.89^{+0.33}_{-0.28}$	$-8.9^{+1.1}_{-1.1}$			
HD 147889	$67.9^{+3.1}_{-2.8}$	$215.3^{+17.1}_{-16.0}$	$7.74^{+0.21}_{-0.21}$	$4.14^{+0.14}_{-0.14}$	$-8.4^{+1.0}_{-1.0}$	tentative detection		H95
HD 147933	$63.4^{+7.4}_{-6.0}$	$165.6^{+43.6}_{-37.0}$	$1.74^{+0.12}_{-0.12}$	$3.67^{+0.33}_{-0.28}$	$-9.2^{+1.1}_{-1.1}$			
HD 148184	$140.7^{+35.4}_{-22.7}$	$222.6^{+29.3}_{-25.6}$	$2.60^{+0.14}_{-0.14}$	$3.74^{+0.28}_{-0.24}$	$-12.7^{+1.1}_{-1.1}$		3.10 ± 0.50	G02
HD 149404 (Comp.1)	$47.4^{+4.9}_{-4.1}$	$243.2^{+79.7}_{-67.1}$	$1.16^{+0.09}_{-0.09}$	$5.25^{+0.80}_{-0.61}$	$-1.2^{+1.3}_{-1.4}$			
HD 149404 (Comp.2)	$66.5^{+10.0}_{-7.5}$	$274.2^{+75.0}_{-60.6}$	$1.10^{+0.10}_{-0.10}$	$4.22^{+0.47}_{-0.40}$	$-20.0^{+1.3}_{-1.3}$			
HD 149757	$72.1^{+8.8}_{-7.0}$	$162.1^{+32.0}_{-27.7}$	$1.60^{+0.10}_{-0.10}$	$4.62^{+0.42}_{-0.35}$	$-15.0^{+1.2}_{-1.2}$		1.60 ± 0.00	O03
							2.01 ± 0.20	G02
							1.83 ± 0.00	R02
							1.60 ± 0.00	M01
HD 152248 [d]	$57.5^{+6.6}_{-5.1}$	$552.0^{+115.0}_{-94.7}$	$1.61^{+0.14}_{-0.14}$	$4.12^{+0.64}_{-0.49}$	$2.3^{+1.2}_{-1.2}$			
HD 154043 [d]	$56.8^{+8.0}_{-6.2}$	$244.1^{+71.3}_{-56.8}$	$1.70^{+0.15}_{-0.15}$	$5.09^{+0.78}_{-0.59}$	$-12.2^{+1.4}_{-1.4}$			
HD 154368	$42.1^{+1.2}_{-1.1}$	$440.4^{+40.4}_{-38.0}$	$4.84^{+0.14}_{-0.14}$	$3.91^{+0.14}_{-0.12}$	$-4.7^{+1.0}_{-1.0}$			
HD 161056 (Comp.1)	$44.5^{+1.5}_{-1.3}$	$913.4^{+78.4}_{-71.2}$	$4.08^{+0.16}_{-0.18}$	$4.92^{+0.33}_{-0.28}$	$-13.2^{+1.1}_{-1.1}$			
HD 161056 (Comp.2)	$42.6^{+3.0}_{-2.6}$	100.0	$1.94^{+0.08}_{-0.09}$	$3.79^{+0.21}_{-0.19}$	$-19.9^{+1.1}_{-1.1}$			
HD 169454	$23.9^{+0.4}_{-0.4}$	1000.0	$6.45^{+0.13}_{-0.13}$	$3.93^{+0.09}_{-0.09}$	$-9.5^{+1.0}_{-1.0}$	22.4 ± 1.0	6.61 ± 0.19	S14
						23.4 ± 1.4	2.24 ± 0.66	A03
							4.30 ± 0.50	O03
HD 179406	$57.2^{+3.7}_{-3.3}$	$105.3^{+20.6}_{-18.7}$	$2.58^{+0.09}_{-0.09}$	$4.24^{+0.21}_{-0.19}$	$-13.2^{+1.1}_{-1.1}$		1.30 ± 0.70	O03
							2.90	R02
							2.00	M01
HD 185859 [d]	$65.1^{+11.3}_{-8.3}$	$220.0^{+71.3}_{-56.1}$	$1.24^{+0.12}_{-0.12}$	$4.59^{+0.71}_{-0.54}$	$-8.1^{+1.3}_{-1.3}$			
HD 186745	$50.2^{+3.6}_{-3.2}$	$315.0^{+63.5}_{-55.6}$	$3.64^{+0.22}_{-0.22}$	$6.45^{+0.94}_{-0.71}$	$-10.8^{+1.4}_{-1.4}$			
HD 186841 (Comp.1)	$72.4^{+9.5}_{-7.3}$	$271.7^{+52.3}_{-44.1}$	$3.12^{+0.22}_{-0.22}$	$5.16^{+0.57}_{-0.47}$	$-11.8^{+1.3}_{-1.3}$			
HD 186841 (Comp.2)	$41.4^{+5.6}_{-4.4}$	$528.2^{+232.7}_{-176.5}$	$1.50^{+0.20}_{-0.20}$	$4.07^{+0.85}_{-0.59}$	$-5.3^{+1.4}_{-1.4}$			
HD 203532	$47.3^{+2.1}_{-1.9}$	$231.1^{+33.1}_{-30.4}$	$2.78^{+0.09}_{-0.09}$	$4.10^{+0.19}_{-0.16}$	$14.2^{+1.1}_{-1.1}$			
HD 210121	$61.8^{+2.9}_{-2.7}$	$140.7^{+15.5}_{-14.5}$	$4.98^{+0.14}_{-0.14}$	$3.86^{+0.12}_{-0.12}$	$-14.7^{+1.0}_{-1.0}$		1.90 ± 0.50	O03
							4.56	R02

Notes. [a]Best-fit results are listed in separate entries for sightline harbouring multiple velocity components. [b]The Gaussian broadening factor FWHM has a lower boundary of 3.00 km s^{-1} to reflect instrumental profile; the fitting boundaries of the excitation temperature for the higher J-levels T_{high} are between 100 and 1000 K; the velocity offset v_{off} is relative to the barycentric frame. [c]Column densities from G02 and R02 have been converted to $f_{000} = 0.016$. The excitation temperature for the lower J-levels is listed if the reference uses double-temperature model. [d]Tentative detection, no individual transition exceeds the 3σ detection limit.

References. H95: Haffner & Meyer (1995); M01: Maier et al. (2001); G02: Galazutdinov et al. (2002); R02: Roueff et al. (2002); A03: Ádámkovics et al. (2003); O03: Oka et al. (2003); S14: Schmidt et al. (2014).

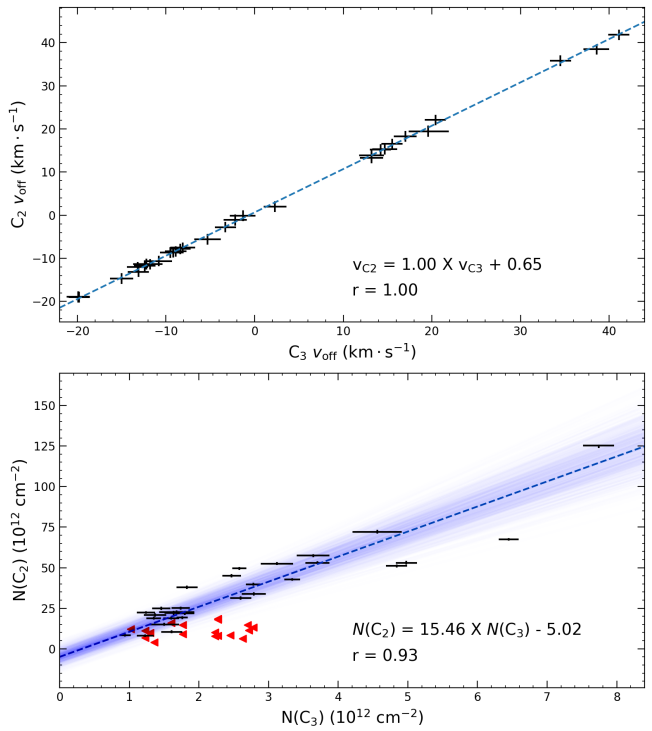

Fig. 4. Comparison between the C_2 and C_3 measurements. Each point represents a velocity component for which both molecules are detected. Upper panel: The velocity offsets of C_2 and C_3 (relative to the barycentric frame) are well aligned, suggesting the two molecules are detected in the same velocity component. Lower panel: $N(C_2)$ and $N(C_3)$ have a good correlation, with $r = 0.93$. The dashed blue line represents the best linear fit from orthogonal distance regression. The 1σ confidence interval of the fit is shown as the shadow. The red triangles represent the 3σ upper limits of $N(C_3)$ in velocity components without C_3 detection. These upper limits are not considered in the linear regression.

with low f_{H2} values (see e.g. Fan et al. 2017, 2019), suggesting that their carriers are not necessarily directly chemically linked to C_2 or other molecules.

In previous sections we carefully examined all 123 EDIBLES targets and detected the C_2 (2-0) Phillips band and the C_3 $\tilde{A} - \tilde{X}$ origin band in a large number of sightlines. The detection of C_2 and C_3 molecules usually suggests dense and molecular environments along the sightlines (see also Appendix C). We refer to the 41 sightlines that show C_2 features as 'C_2 sightlines' and the rest as 'non-C_2 sightlines'. This section discusses how C_2 and non-C_2 DIBs behave in these sightlines. Since DIB measurements are not the primary focus of this work, we adopted the DIB equivalent widths (W(DIBs)) from Fan et al. (2017). Readers are referred to the original paper for details on how the measurements were obtained.

Figure 5 compares the general behaviour of four DIBs, in terms of W(DIBs) – E_{B-V} correlations, between the C_2 and non-C_2 sightlines. The comparisons are made for two non-C_2 DIBs $\lambda\lambda$5780 and 6196, and two of the well-recognised C_2 DIBs $\lambda\lambda$4963 and 4984. Both non-C_2 DIBs have reduced strengths in the C_2 sightlines, which was described as the 'skin effect' in early DIB observations (e.g. Wampler 1966; Strom et al. 1975; Meyer & Ulrich 1984; Herbig 1995). This observational fact suggests that the inner parts of the clouds have a limited contribution to the column density of the general DIB material (Snow & Cohen 1974). As a more quantitative analysis, Fan et al. (2017) reported 'lambda-shaped' behaviour of non-C_2 DIBs where their normalised strengths (W(DIB)/E_{B-V}) decrease as a function of f_{H2} for $f_{H2} > \sim 0.3$. This is also approximately the range of the f_{H2} values for the C_2 sightlines we identified (Appendix C).

In direct contrast, the C_2 DIBs $\lambda\lambda$4963 and 4984 showed undifferentiated behaviour among C_2 and non-C_2 sightlines. This is consistent with the observations that $W(C_2\ \mathrm{DIBs})/E_{B-V}$ remains relatively constant (with large scatter) in sightlines with large f_{H2} values (Fan et al. 2017). The C_2 DIBs are originally defined by an enhanced ratio of $W(C_2\ \mathrm{DIBs})/W(6196)$ in the C_2 sightlines (Thorburn et al. 2003). This increment is more likely the result of decreased W(6196) rather than increased $W(C_2$ DIBs), and provides evidence that the C_2 DIBs may trace denser environments than the non-C_2 DIBs. However, since the C_2 DIBs are not enhanced in the C_2 sightlines, their carriers may not reside in the deep layers of the ISM clouds where C_2 and other second-generation molecules are found (e.g. CN and CO; see Fan et al. 2022).

7. One step further: Search for more complicated carbon chains

7.1. Rare C_2 isotopologue ($^{13}C^{12}C$)

The positions of the transitions from the $^{13}C^{12}C$ (0-0) and (1-0) Phillips $A\,^1\Pi$–$X\,^1\Sigma^+$ bands were first provided by Amiot & Verges (1983) using Fourier spectroscopy. Hamano et al. (2019) recently reported the first tentative detection of $^{13}C^{12}C$ in the ISM using these data. This marginal detection is for the $Q(3)$ transition of the (0-0) band and is made towards the heavily reddened sightline of Cyg OB2 12. To the best of our knowledge, no dedicated laboratory studies are yet available on the $^{13}C^{12}C$ (2-0) bands. We calculated the required transition wavelengths and f_{jj} values using the well-known isotopic dependence of the Dunham vibration-rotation coefficients (Watson 1980).

For this purpose, we followed the same approach as described in Ram et al. (2014) and Rousselot et al. (2012) and utilised the molecular parameters of the main $^{12}C_2$ isotopologue (Chen et al. 2015) and the isotopic relationships (Ram et al. 2014; Rousselot et al. 2012; Watson 1980):

$$
\begin{aligned}
&\omega'_e = \rho\omega_e \\
&\omega_e x'_e = \rho^2 \omega_e x_e \\
&\omega_e y'_e = \rho^3 \omega_e y_e \\
&\omega_e z'_e = \rho^4 \omega_e z_e \\
&\omega_e a'_e = \rho^5 \omega_e a_e \\
&B'_e = \rho^2 B_e \\
&\alpha'_e = \rho^3 \alpha_e \\
&\gamma'_e = \rho^4 \gamma_e \\
&\delta'_e = \rho^5 \delta_e \\
&\epsilon'_e = \rho^6 \epsilon_e \\
&D'_e = \rho^4 D_e \\
&\beta'_e = \rho^5 \beta_e \\
&\zeta'_e = \rho^6 \zeta_e \\
&q' = \rho^4 q, \\
&\alpha^{q\prime} = \rho^5 \alpha^q \\
&q'_D = \rho^8 q_D.
\end{aligned}
\tag{3}
$$

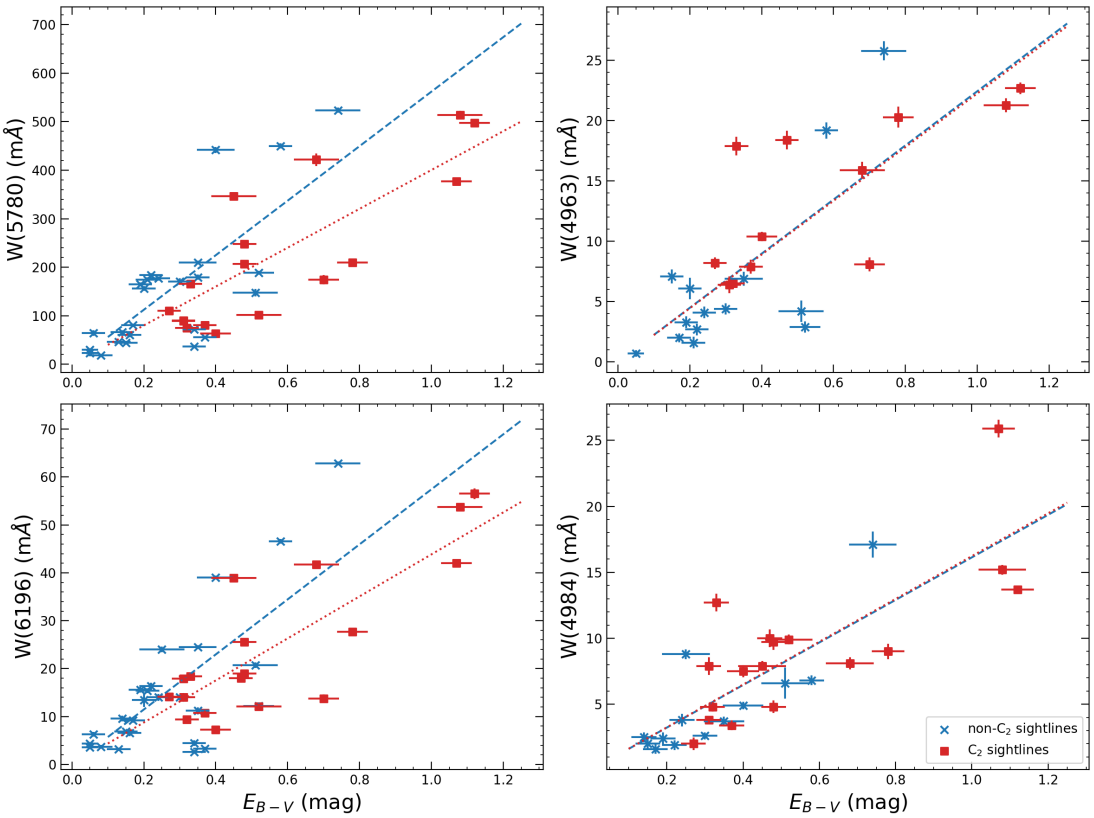

Fig. 5. Behaviour of non-C_2 DIBs $\lambda\lambda$5780 and 6196 (left panels), and C_2 DIBs $\lambda\lambda$4963 and 4984 (right panels) in C_2 and non-C_2 sightlines. The non-C_2 DIBs show the 'skin effect' and have reduced strengths in the C_2 sightlines. However, the behaviour of the C_2 DIBs is rather similar in the two types of sightlines. They may trace deeper regions of a cloud than the non-C_2 DIBs, but not as deep as the C_2 molecules. The DIB equivalent width data are gathered from Fan et al. (2017).

Table 4. Mass-scaled spectroscopic constants of $^{13}C^{12}C$ in the (2-0) Phillips system.

Constants [a]	$X\,^1\Sigma^+(v=0)$		$A\,^1\Pi(v=2)$
	This work [b]	Literature [c]	This work [b]
Band origin			11354.65876
B_v	1.74133	1.741417	1.51402
$D_v \times 10^6$	6.46215	6.530	6.06544
$q_v \times 10^4$			−1.77837
$q_D \times 10^9$			4.31457

Notes. All values are in cm^{-1}. [a]B_v and D_v are rotational and centrifugal distortion parameters, while q_v and q_D are Λ-type doubling constants. v define vibrational quantum numbers; see Chen et al. (2015) for details. [b]Calculated from $^{12}C_2$ (Chen et al. 2015) and isotopic relations (see the main text). [c]Laboratory spectroscopic data; see Amiot & Verges (1983).

Here the primed and unprimed quantities are equilibrium spectroscopic constants for $^{13}C^{12}C$ and $^{12}C_2$, respectively (as defined in Chen et al. 2015) and $\rho = \sqrt{\mu_{\rm main}/\mu_{\rm rare}} = 0.98052$, with the μ being the reduced mass. The resulting primed (equilibrium) constants of $^{13}C^{12}C$ (Eq. (3)) were then used as input into standard spectroscopic formulas (see e.g. pages 3–4 Chen et al. 2015) to introduce the proper vibrational dependence into the relevant mass-scaled parameters. Their final values are gathered in Table 4. The list with calculated line positions was subsequently generated using the final spectroscopic constants in Table 4 and PGOPHER (see Table 5; Western 2017).

We employed the methodology described in Ram et al. (2014) to determine the f_{jj} values for the $^{13}C^{12}C$ (2-0) Phillips bands. Briefly, the potential energy curves for each electronic state are represented by Rydberg-Klein-Rees (RKR) classical turning points (Le Roy 2014). These are calculated using the RKR1 program (Le Roy 2014) and the mass-scaled spectroscopic constants of the upper ($A\,^1\Pi$) and lower ($X\,^1\Sigma^+$) $^{13}C^{12}C$ states (Eq. (3)). With the corresponding ab initio electronic transition dipole moment function reported by Yurchenko et al. (2018), Einstein A-coefficients ($A_{J'\rightarrow J''}$) were then determined using the LEVEL code (Le Roy 2017), and finally converted into the f_{jj} values following the usual expression (Ram et al. 2014):

$$f_{J'\leftarrow J''} = 1.49919368 \frac{1}{\tilde{\nu}^2} \frac{(2J'+1)}{(2J''+1)} A_{J'\rightarrow J''}. \quad (4)$$

Here, $\tilde{\nu}$ is the transition wavenumber (in cm^{-1}) associated with the lower (J'') and upper (J') ro-vibronic J states.

Unlike the regular C_2 molecule, $^{13}C^{12}C$ has additional transitions from odd J-levels due to its hetero-nuclear nature. Our simulation suggests that the $Q(1)$ – $Q(4)$ transitions are the strongest under typical excitation conditions with $T_{\rm exc} \sim$ 60 K. Their calculated wavelengths and f_{jj} values are summarised in Table 5. We also included the calculated (following the same approach described above) f_{jj} values of the regular $^{12}C_2$ molecule for comparison. As expected, they differ by less than 1.2%. We also note that our calculated f_{jj} values for the $^{12}C_2$ molecule reproduce to within 0.4% those reported by Sonnentrucker et al. (2007), hence further supporting the reliability of our approach.

Table 5. Calculated line list of the $^{13}C^{12}C$ (2-0) Phillips band.

Transition	λ_{jj} [a,b] (Å)	f_{jj} ($\times 10^4$)		
		$^{13}C^{12}C$ [b]	$^{12}C_2$ [b]	Literature [c]
$Q(1)$	8804.892	7.11	–	–
$Q(2)$	8805.597	7.11	7.03	7.00
$Q(3)$	8806.655	7.11	–	–
$Q(4)$	8808.065	7.11	7.03	7.00

Notes. [a]Air wavelength. [b]Calculated from molecular constants of $^{12}C_2$ (Chen et al. 2015) and isotopic relations. See the main text for more details. [c]f_{jj} values of $^{12}C_2$ from Sonnentrucker et al. (2007).

We focused on the sightlines of HD 63804, HD 147889, and HD 169454 because of their large C_2 column densities and good S/N in the target region. These factors make them plausible candidates to search for the $^{13}C^{12}C$ transitions, yet we cannot make robust detection on the target $^{13}C^{12}C$ transitions in any of these sightlines (Fig. 6, upper panel). To further increase the sensitivity of our data, we continued by performing a S/N-weighted spectral stacking for the three sightlines. The measured S/N of the stacked spectrum reaches ~3000, and the $Q(2)$, $Q(3)$, and $Q(4)$ transitions are detected in the stacked spectrum (Fig. 6, lower panel). This detection validates our theoretical prediction on the wavelengths, which is based solely on isotopic relations (Rousselot et al. 2012; Ram et al. 2014).

The stacking process, however, averages different ISM conditions of the three sightlines, and we cannot obtain detailed excitation information for $^{13}C^{12}C$ in the stacked data. Because of this, the best approach to even calculating the column density of $^{13}C^{12}C$ requires analysis of a wide range of probable excitation conditions especially regarding the excitation temperature. We compiled a series of models with T_{exc} between 40 and 80 K (with an interval of 5 K), and obtained the relative strengths of the $Q(1)$ to $Q(4)$ transitions from PGOPHER. We assumed a Gaussian profile with instrumental widths for each of the transitions. The best fit with the minimal χ^2 occurs when T_{exc} = 55 K with $N(^{13}C^{12}C) = 2.30 \times 10^{12}$ cm^{-2}. The standard deviation of $N(^{13}C^{12}C)$ among models of different T_{exc} is 0.31×10^{12} cm^{-2} (~13%), representing the uncertainty due to the unknown excitation conditions.

The average $N(C_2)$ is 8.92×10^{13} cm^{-2} for the three sightlines[4]. The $N(C_2)/N(^{13}C^{12}C)$ ratio is then ~39 ± 4, or a $^{12}C/^{13}C$ ratio of ~79 ± 8. This is very close to the same ratio of 72±26 observed towards the circumstellar shell of the post-asymptotic-giant-branch star HD 56126 (Bakker & Lambert 1998). The $^{12}C/^{13}C$ ratio can also be obtained from other carbon-bearing molecules. For examples, Milam et al. (2005) reported ~68 by considering CO, H_2CO, and CN, and Stahl et al. (2008) find 76±2 using CH^+ measurements of the local ISM. Again the findings of this work are well aligned with the above literature results.

The $^{12}C/^{13}C$ ratio traces the large-scale Galactic chemical evolution as well as local peculiarities of the ISM conditions (e.g. Milam et al. 2005; Furuya et al. 2011; Liszt & Ziurys 2012). Rocha & Linnartz (2021) discussed the temperature dependence

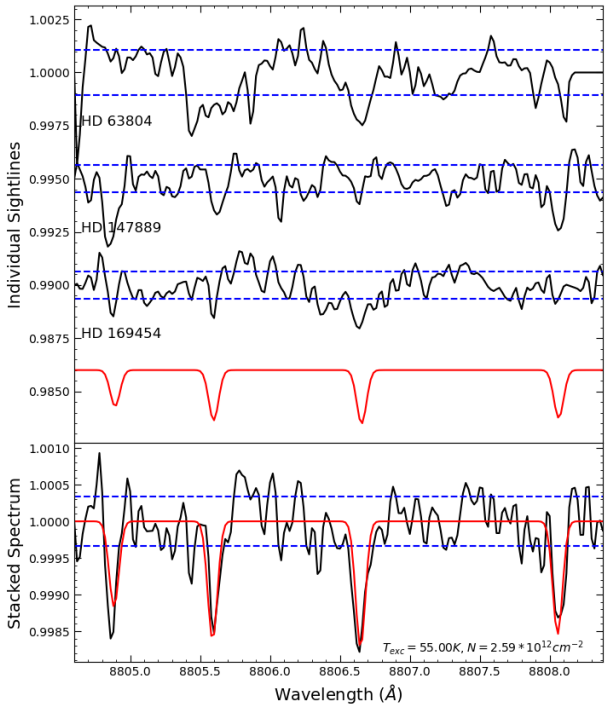

Fig. 6. Search for $^{13}C^{12}C$ (2-0) Phillips transitions. Top panel: spectral segments of HD 63804, HD 147889, and HD 169454 around the target wavelength region, and simulated data (red) for $^{13}C^{12}C$ with T_{exc} = 55 K. From left to right, the four transitions are $Q(1)$, $Q(2)$, $Q(3)$, and $Q(4)$. Unfortunately, we cannot identify these features in any individual sightline. Bottom panel: stacked (average) data of the three sightlines. We have a 3σ detection of the $Q(2)$ and $Q(3)$ transitions, and a marginal detection of the $Q(4)$ transition. The estimated column density of $^{13}C^{12}C$ is $2.30 \pm 0.31 \times 10^{12}$cm^{-2} in the stacked spectrum, corresponding to a $^{12}C/^{13}C$ ratio of 79±8. The dashed blue lines around the spectra represent 1σ uncertainties.

of the isotopic fractionation of carbon. Their calculation suggests that a smaller $^{12}C/^{13}C$ ratio can be expected in sightlines characterised by lower kinetic temperature, since the forward isotope-exchange reaction $^{13}C + {}^{12}C_2 \rightarrow {}^{13}C^{12}C + {}^{12}C$ is exothermic by 26.4 K and the reverse endothermic process becomes largely inefficient at low temperatures. We note in passing that the $^{13}C^+ + {}^{12}C_2$ reaction, despite not being considered by Rocha & Linnartz (2021) in the context of dense molecular clouds, is also expected to play a key contribution to the overall carbon isotopic fractionation, particularly under the diffuse ISM environments (Loison et al. 2020; Colzi et al. 2020). Compared to T_{kin} = 20 K, the $^{12}C/^{13}C$ ratio can be a factor of 2 greater when T_{kin} = 100 K. The identification in stacked data cannot assign the $^{12}C/^{13}C$ ratio to specific ISM conditions, but such dependences may be examined in future studies.

7.2. C_4 and C_5

The C_4 and C_5 molecules are the simplest bare carbon chains after C_2 and C_3. In the optical region, the strongest C_4 band occurs at 3789 Å and is between the $^3\Sigma_u^-$ and $^3\Sigma_g^-$ states. The laboratory spectrum of this band is characterised by the piled-up R-branch to the blue and more expanding P-branch contour to the red (Linnartz et al. 2000; Fig. 7, left panel). The strongest C_5 optical band is at 5109 Å and Forney et al. (1996) assigned this band to the $^1\Pi_u - X^1\Sigma_g^+$ system. However, Hanrath & Peyerimhoff (2001) noted a discrepancy of ~0.5 eV in the transition

[4] During the stacking process, the spectral data were weighted by their S/Ns. The same weight was applied to calculate the average $N(C_2)$ in the three sightlines. We also tried to measure $N(C_2)$ in the stacked spectrum around the $^{12}C_2$ transitions, but the fitting was unsuccessful due to the mixture of ISM conditions.

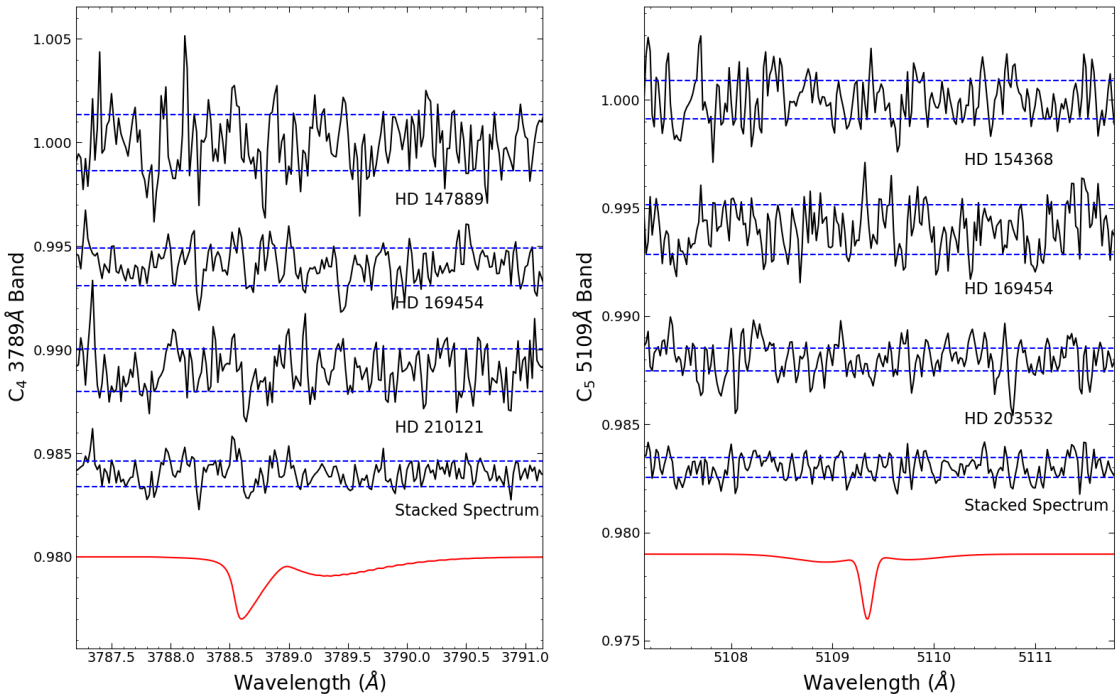

Fig. 7. Spectral data around the C_4 $^3\Sigma_u^- - ^3\Sigma_g^-$ 3789 Å band (left) and the C_5 5109 Å band, possibly from the $^1\Pi_u - X^1\Sigma_g^+$ system (right). Their lab spectra are shown at the bottom as reference (red). The sightlines are selected by their measured $N(C_3)$ and the S/N of the wavelength region, which is indicated by the dashed blue lines. We cannot find the target transition in either individual sightlines nor their stacked spectrum. Upper limits on $N(C_4)$ and $N(C_5)$ can be estimated from their most prominent feature, and are around 10^{13} cm^{-2} and 10^{12} cm^{-2}, respectively.

Table 6. Upper limits of $N(C_4)$ and $N(C_5)$.

Species		Sightlines			
		HD 147889	HD 169454	HD 210121	Stacked
C_4	λ_{jj} (Å)	3789			
	FWHM$^{(a,b)}$ (Å)	0.24			
	f_{jj} $^{(b)}$	0.0006			
	W_{max} $^{(c)}$ (mÅ)	2.1	1.7	1.6	1.0
	N_{max} (cm^{-2})	2.7×10^{13}	1.8×10^{13}	2.1×10^{13}	1.2×10^{13}
	$N(C_3)/N_{max}$	0.28	0.35	0.23	0.50
		HD 154368	HD 169454	HD 203532	Stacked
C_5	λ_{jj} (Å)	5109			
	FWHM$^{(a,b)}$ (Å)	0.13			
	f_{jj} $^{(b)}$	0.001			
	W_{max} $^{(c)}$ (mÅ)	0.74	0.84	0.44	0.39
	N_{max} (cm^{-2})	5.9×10^{12}	7.6×10^{12}	3.6×10^{12}	3.1×10^{12}
	$N(C_3)/N_{max}$	0.81	1.18	0.78	0.66

Notes. $^{(a)}$For the most prominent feature. $^{(b)}$From Maier et al. (2002). $^{(c)}$Assuming the most prominent feature has Gaussian profile and contributes to half of the total absorption.

energy and suggested the 5109 Å band to be associated with formally forbidden $^1\Sigma_u^-$ and $^1\Delta_u$ states. Nevertheless the most prominent feature of this band is the piled-up Q-branch in the middle while the contours of the P- and Q-branches are much shallower (Fig. 7, right panel).

Similar to our search for $^{13}C^{12}C$, we searched for these optical bands of C_4 and C_5 in candidate sightlines characterised by large $N(C_3)$ and high S/N in the wavelength region (namely, HD 147889, HD 169454, and HD 210121 for the C_4 3789 Å band and HD 154368, HD 169454, and HD 203532 for the C_5 5109 Å band). However, neither of the target transitions can be identified in individual sightlines or their stacked spectra (Fig. 7). We instead estimated the upper limits of $N(C_4)$ and $N(C_5)$ by considering the most prominent feature in their band profile (i.e. the R-branch contour for C_4 3789 Å band and the Q-branch contour for C_5 5109 Å band) while assuming it contributes 50% of the total absorption. The results are summarised in Table 6.

The C_5 molecules have been detected in earlier work via their IR transitions in the carbon-rich circumstellar shell around IRC +10216. Bernath et al. (1989) suggested $N(C_5)$ might be ∼1/10 of $N(C_3)$, yet a more recent observation provided a much smaller

$N(C_5)/N(C_3)$ ratio of 1/68 (Hargreaves et al. 2014). Theoretical models also predict $N(C_4)$ and $N(C_5)$ to be one to two orders of magnitude smaller than $N(C_3)$ (e.g. Terzieva & Herbst 1998; Schmidt et al. 2014), and the much smaller f_{jj} values of the C_4 and C_5 optical bands make their detection even more difficult. These f_{jj} values are also inconsistent in the literature. For example, Mühlhäuser et al. (2000) reported $f_{jj} \sim 0.0001$ for the C_4 3789 Å band, which is merely one-sixth of the value used in Table 6 (see also Jungen & Xu 2003; Pacchioni & Koutecký 1988). Under the best case scenario where $N(C_4)$ and $N(C_5)$ is ∼1/10 of $N(C_3)$ and their transitions have the largest f_{jj} values reported in the literature, the S/N of the most molecule-rich sightlines should be boosted by a factor of 2–10 to increase the chance for a successful C_4 or C_5 detection.

8. Summary

We conducted an extensive survey of C_2 and C_3 signatures in the EDIBLES dataset, using the C_2 $A^1\Pi_u \leftarrow X^1\Sigma_g^+$ (2-0) Phillips band and the C_3 $\tilde{A}\ ^1\Pi_u - \tilde{X}^1\Sigma_g^+$ 000-000 electronic origin band. Our data have high S/N and can resolve individual ro-vibronic transitions of the above bands, which allowed us to characterise the rotational excitation and obtain more accurate column densities. The results and conclusions we have reached are as follows:

1. We detect the C_2 (2-0) Phillips band in 51 velocity components along 40 sightlines; 48 velocity components have detections at the 3σ level or better, and three sightlines have tentative detections. The data were interpreted following the excitation model of van Dishoeck & Black (1982), and we were able to obtain information about the kinetic temperature and density in addition to the column density.
2. We detect the C_3 $\tilde{A} - \tilde{X}$ 000-000 band in 31 velocity components along 27 sightlines; 23 velocity components in 19 sightlines have detections at the 3σ level or better, and eight sightlines have tentative detections of C_3. Due to the lack of a detailed excitation model, we assumed a double-temperature Boltzmann distribution and report the excitation temperatures and column density.
3. The C_2 and C_3 transitions have consistent velocity offsets within their uncertainties, suggesting that the two species are detected in the same velocity components. We find a good correlation between $N(C_2)$ and $N(C_3)$, namely $r = 0.93$. The average $N(C_2)/N(C_3)$ ratio in our survey is 15.5±1.4, which is lower than a previously reported value of ∼40 (where individual C_3 transitions were not resolved) and slightly higher than the value of ∼10 reported by Schmidt et al. (2014).
4. We confirm that the C_2/C_3 detections occur in ζ-type sightlines characterised by large f_{H2} values and low $W(5780)/W(5797)$ ratios. We compared the behaviour of DIBs in C_2 and non-C_2 sightlines. Unlike regular DIBs, the C_2 DIBs exhibit a similar behaviour in the two types of sightlines. They may trace denser regions in the ISM clouds than the regular DIBs, yet not as deep as where C_2 molecules are found.
5. We searched for the optical bands of C_4, C_5, and the singly substituted isotopologue of C_2 ($^{13}C^{12}C$) in sightlines with high C_2/C_3 column densities. We identified the $^{13}C^{12}C$ (2-0) Phillips band in a stacked spectrum via its $Q(2)$, $Q(3)$, and (tentatively) $Q(4)$ transitions. The estimated $^{12}C/^{13}C$ ratio is 79±8. For C_4 and C_5, only upper limits to the column density can be derived, as in earlier unsuccessful surveys.

The high spectral resolution and high S/N offered by the EDIBLES dataset thus result in accurate determinations of the physical parameters that describe the denser parts of diffuse clouds, and provides us with insight into the chemistry in these regions.

Acknowledgements. H.F. and J.C. acknowledge support from an NSERC Discovery Grant and a Western SERB Accelerator Award. C.M.R.R. gratefully acknowledges the financial support from the European Union's Horizon 2020 research and innovation program under the Marie Skłodowska-Curie grant agreement no. 894321.

References

Ádámkovics, M., Blake, G. A., & McCall, B. J. 2003, ApJ, 595, 235
Amiot, C., & Verges, J. 1983, A&AS, 51, 257
Bacalla, X. L., Linnartz, H., Cox, N. L. J., et al. 2019, A&A, 622, A31
Bakker, E. J., & Lambert, D. L. 1998, ApJ, 508, 387
Bakker, E. J., van Dishoeck, E. F., Waters, L. B. F. M., & Schoenmaker, T. 1997, A&A, 323, 469
Becker, K. H., Tatarczyk, T., & Radić-Perić, J. 1979, Chem. Phys. Lett., 60, 502
Bergeat, A., & Loison, J.-C. 2001, Phys. Chem. Chem. Phys., 3, 2038
Bernath, P. F., Hinkle, K. H., & Keady, J. J. 1989, Science, 244, 562
Cami, J., Sonnentrucker, P., Ehrenfreund, P., & Foing, B. H. 1997, A&A, 326, 822
Cami, J., Salama, F., Jiménez-Vicente, J., Galazutdinov, G. A., & Krełowski, J. 2004, ApJ, 611, L113
Campbell, E. K., Holz, M., Gerlich, D., & Maier, J. P. 2015, Nature, 523, 322
Casu, S., & Cecchi-Pestellini, C. 2012, ApJ, 749, 48
Cernicharo, J., Goicoechea, J. R., & Caux, E. 2000, ApJ, 534, L199
Cernicharo, J., Goicoechea, J. R., & Benilan, Y. 2002, ApJ, 580, L157
Chen, W., Kawaguchi, K., Bernath, P. F., & Tang, J. 2015, J. Chem. Phys., 142, 064317
Colzi, L., Sipilä, O., Roueff, E., Caselli, P., & Fontani, F. 2020, A&A, 640, A51
Cordiner, M. A., Linnartz, H., Cox, N. L. J., et al. 2019, ApJ, 875, L28
Cox, N. L. J., & Patat, F. 2014, A&A, 565, A61
Cox, N. L. J., Cami, J., Farhang, A., et al. 2017, A&A, 606, A76
Crawford, I. A. 1997, MNRAS, 290, 41
Dekker, H., D'Odorico, S., Kaufer, A., Delabre, B., & Kotzlowski, H. 2000, SPIE Conf. Ser., 4008, 534
Douglas, A. E. 1951, ApJ, 114, 466
Ebenbichler, A., Postel, A., Przybilla, N., et al. 2022, A&A, 662, A81
Elyajouri, M., Lallement, R., Cox, N. L. J., et al. 2018, A&A, 616, A143
Fan, H., Welty, D. E., York, D. G., et al. 2017, ApJ, 850, 194
Fan, H., Hobbs, L. M., Dahlstrom, J. A., et al. 2019, ApJ, 878, 151
Fan, H., Schwartz, M., Farhang, A., et al. 2022, MNRAS, 510, 3546
Federman, S. R., & Huntress, W. T., J. 1989, ApJ, 338, 140
Federman, S. R., Strom, C. J., Lambert, D. L., et al. 1994, ApJ, 424, 772
Federman, S. R., Rice, J. S., Ritchey, A. M., et al. 2021, ApJ, 914, 59
Foing, B. H., & Ehrenfreund, P. 1994, Nature, 369, 296
Forney, D., Freivogel, P., Grutter, M., & Maier, J. P. 1996, J. Chem. Phys., 104, 4954
Freeman, P., Doe, S., & Siemiginowska, A. 2001, SPIE Conf. Ser., 4477, 76
Furuya, K., Aikawa, Y., Sakai, N., & Yamamoto, S. 2011, ApJ, 731, 38
Galazutdinov, G., Pětlewski, A., Musaev, F., et al. 2002, A&A, 395, 969
Gausset, L., Herzberg, G., Lagerqvist, A., & Rosen, B. 1965, ApJ, 142, 45
Geballe, T. R., Najarro, F., Figer, D. F., Schlegelmilch, B. W., & de La Fuente, D. 2011, Nature, 479, 200
Giesen, T. F., Mookerjea, B., Fuchs, G. W., et al. 2020, A&A, 633, A120
Gredel, R. 1999, A&A, 351, 657
Gredel, R. 2004, A&A, 425, 151
Gredel, R., Black, J. H., & Yan, M. 2001, A&A, 375, 553
Gredel, R., Carpentier, Y., Rouillé, G., et al. 2011, A&A, 530, A26
Haddad, M., Zhao, D., Linnartz, H., & Ubachs, W. 2014, J. Mol. Spectrosc., 297, 41
Haffner, L. M., & Meyer, D. M. 1995, ApJ, 453, 450
Hamano, S., Kawakita, H., Kobayashi, N., et al. 2019, ApJ, 881, 143
Hanrath, M., & Peyerimhoff, S. D. 2001, Chem. Phys. Lett., 337, 368
Hargreaves, R. J., Hinkle, K., & Bernath, P. F. 2014, MNRAS, 444, 3721
Heger, M. L. 1922, Lick Observ. Bull., 10, 146
Herbig, G. H. 1995, ARA&A, 33, 19
Hinkle, K. W., Keady, J. J., & Bernath, P. F. 1988, Science, 241, 1319
Hobbs, L. M., & Campbell, B. 1982, ApJ, 254, 108
Hobbs, L. M., Black, J. H., & van Dishoeck, E. F. 1983, ApJ, 271, L95
Hobbs, L. M., York, D. G., Snow, T. P., et al. 2008, ApJ, 680, 1256

Hobbs, L. M., York, D. G., Thorburn, J. A., et al. 2009, ApJ, 705, 32
Hrodmarsson, H. R., Bouwman, J., Tielens, A. G. M., & Linnartz, H. 2022, Int. J. Mass Spectr., 476, 116834
Huggins, W. 1881, Proc. R. Soc. London Ser., 33, 1
Hupe, R. C., Sheffer, Y., & Federman, S. R. 2012, ApJ, 761, 38
Iglesias-Groth, S. 2011, MNRAS, 411, 1857
Jungen, C., & Merer, A. J. 1980, Mol. Phys., 40, 95
Jungen, M., & Xu, R. 2003, Zeitschrift für Physikalische Chemie, 217, 105
Kaźmierczak, M., Schmidt, M. R., Bondar, A., & Krełowski, J. 2010a, MNRAS, 402, 2548
Kaźmierczak, M., Schmidt, M. R., Galazutdinov, G. A., et al. 2010b, MNRAS, 408, 1590
Kerr, T. H., Hibbins, R. E., Fossey, S. J., Miles, J. R., & Sarre, P. J. 1998, ApJ, 495, 941
Kokkin, D. L., Bacskay, G. B., & Schmidt, T. W. 2007, J. Chem. Phys., 126, 084302
Kos, J., & Zwitter, T. 2013, ApJ, 774, 72
Lallement, R., Cox, N. L. J., Cami, J., et al. 2018, A&A, 614, A28
Le Roy, R. J. 2014, RKR1 2.0: A Computer Program Implementing the First-Order RKR Method for Determining Diatomic Molecule Potential Energy Functions, University of Waterloo, Chemical Physics Research Report CP-657R (2004); see http://leroy.uwaterloo.ca
Le Roy, R. J. 2017, J. Quant. Spectrosc. Radiat. Transf., 186, 167
Linnartz, H., Vaizert, O., Motylewski, T., & Maier, J. P. 2000, J. Chem. Phys., 112, 9777
Liszt, H. S., & Ziurys, L. M. 2012, ApJ, 747, 55
Loison, J.-C., Wakelam, V., Gratier, P., & Hickson, K. M. 2020, MNRAS, 498, 4663
MacIsaac, H., Cami, J., Cox, N. L. J., et al. 2022, A&A, 662, A24
Maier, J. P., Lakin, N. M., Walker, G. A. H., & Bohlender, D. A. 2001, ApJ, 553, 267
Maier, J. P., Walker, G. A. H., & Bohlender, D. A. 2002, ApJ, 566, 332
Maier, J. P., Walker, G. A. H., & Bohlender, D. A. 2004, ApJ, 602, 286
Martin-Drumel, M.-A., Zhang, Q., Doney, K. D., et al. 2023, J. Mol. Spectr., 391, 111734
McCall, B. J., Casaes, R. N., Ádámkovics, M., & Saykally, R. J. 2003, Chem. Phys. Lett., 374, 583
Meyer, D. M., & Ulrich, R. K. 1984, ApJ, 283, 98
Milam, S. N., Savage, C., Brewster, M. A., Ziurys, L. M., & Wyckoff, S. 2005, ApJ, 634, 1126
Mookerjea, B., Giesen, T., Stutzki, J., et al. 2010, A&A, 521, L13
Motylewski, T., Linnartz, H., Vaizert, O., et al. 2000, ApJ, 531, 312
Mühlhäuser, M., Froudakis, G. E., Hanrath, M., & Peyerimhoff, S. D. 2000, Chem. Phys. Lett., 324, 195
Oka, T., Thorburn, J. A., McCall, B. J., et al. 2003, ApJ, 582, 823
Oka, T., Welty, D. E., Johnson, S., et al. 2013, ApJ, 773, 42
Pacchioni, G., & Koutecký, J. 1988, J. Chem. Phys., 88, 1066
Perić-Radić, J., Römelt, J., Peyerimhoff, S. D., & Buenker, R. J. 1977, Chem. Phys. Lett., 50, 344
Ram, R. S., Brooke, J. S. A., Bernath, P. F., Sneden, C., & Lucatello, S. 2014, ApJS, 211, 5
Rocha, C. M. R., & Linnartz, H. 2021, A&A, 647, A142
Rothman, L. S. 2021, Nat. Rev. Phys., 3, 302
Roueff, E., Felenbok, P., Black, J. H., & Gry, C. 2002, A&A, 384, 629
Rousselot, P., Jehin, E., Manfroid, J., & Hutsemékers, D. 2012, A&A, 545, A24
Salama, F., & Ehrenfreund, P. 2014, IAU Symp., 297, 364
Salama, F., Galazutdinov, G. A., Krełowski, J., et al. 2011, ApJ, 728, 154
Sarre, P. J., Miles, J. R., Kerr, T. H., et al. 1995, MNRAS, 277, L41
Schmidt, M. R., Krełowski, J., Galazutdinov, G. A., et al. 2014, MNRAS, 441, 1134
Smoker, J., Haddad, N., Iwert, O., et al. 2009, The Messenger, 138, 8
Snow, T. P., J., & Cohen, J. G. 1974, ApJ, 194, 313
Snow, T. P., & McCall, B. J. 2006, ARA&A, 44, 367
Sonnentrucker, P., Cami, J., Ehrenfreund, P., & Foing, B. H. 1997, A&A, 327, 1215
Sonnentrucker, P., Welty, D. E., Thorburn, J. A., & York, D. G. 2007, ApJS, 168, 58
Souza, S. P., & Lutz, B. L. 1977, ApJ, 216, L49
Stahl, O., Casassus, S., & Wilson, T. 2008, A&A, 477, 865
Strom, K. M., Strom, S. E., Carrasco, L., & Vrba, F. J. 1975, ApJ, 196, 489
Tanabashi, A., Hirao, T., Amano, T., & Bernath, P. F. 2005, ApJ, 624, 1116
Terzieva, R., & Herbst, E. 1998, ApJ, 509, 932
Thorburn, J. A., Hobbs, L. M., McCall, B. J., et al. 2003, ApJ, 584, 339
van Dishoeck, E. F., & Black, J. H. 1982, ApJ, 258, 533
van Dishoeck, E., & Black, J. H. 1986, ApJ, 307, 332
van Dishoeck, E. F., & Black, J. H. 1989, ApJ, 340, 273
van Dishoeck, E. F., & de Zeeuw, T. 1984, MNRAS, 206, 383
Visser, R., van Dishoeck, E. F., & Black, J. H. 2009, A&A, 503, 323
Vos, D. A. I., Cox, N. L. J., Kaper, L., Spaans, M., & Ehrenfreund, P. 2011, A&A, 533, A129
Wakelam, V., Loison, J. C., Herbst, E., et al. 2009, A&A, 495, 513
Walker, G. A. H., Bohlender, D. A., Maier, J. P., & Campbell, E. K. 2015, ApJ, 812, L8
Wampler, E. J. 1966, ApJ, 144, 921
Watson, J. K. 1980, J. Mol. Spectrosc., 80, 411
Wehres, N., Romanzin, C., Linnartz, H., van Winckel, H., & Tielens, A. G. G. M. 2010, A&A, 518, A36
Welty, D. E., Howk, J. C., Lehner, N., & Black, J. H. 2013, MNRAS, 428, 1107
Welty, D. E., Sonnentrucker, P., Snow, T. P., & York, D. G. 2020, ApJ, 897, 36
Western, C. M. 2017, J. Quant. Spectrosc. Radiat. Transf., 186, 221
Yurchenko, S. N., Szabó, I., Pyatenko, E., & Tennyson, J. 2018, MNRAS, 480, 3397
Zack, L. N., & Maier, J. P. 2014, Chem. Soc. Rev., 43, 4602
Zhang, G., Chen, K.-S., Merer, A. J., et al. 2005, J. Chem. Phys., 122, 244308

Appendix A: Fitted C_2 models

In this appendix we present plots of the best-fit model of the C_2 (2-0) Phillips band compared to the normalised flux for the 40 sightlines listed in Table C.1. Readers are referred to Sect. 3 for details about the model.

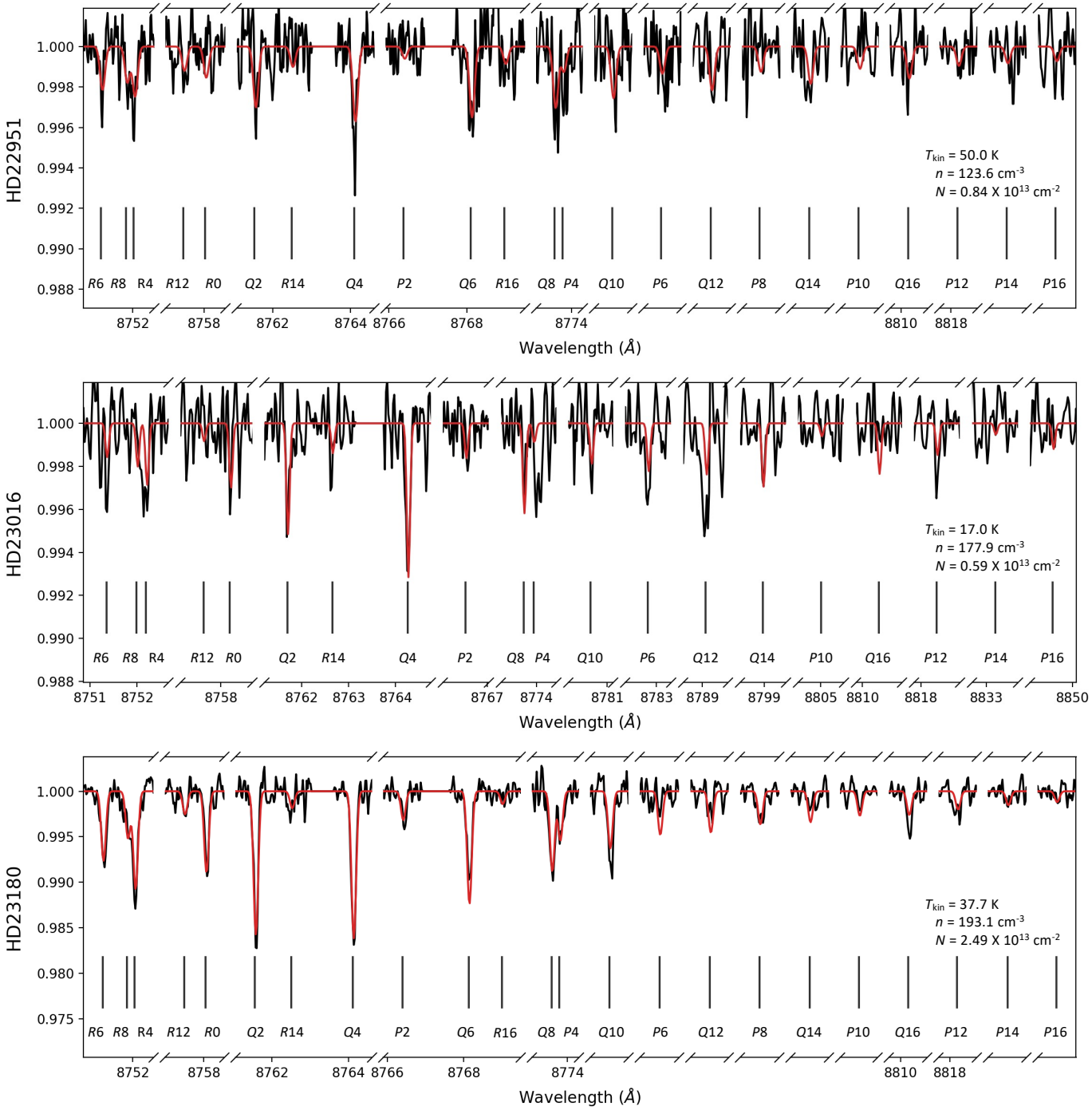

Fig. A.1. Normalised flux (black) and fitted model of the C_2 (2-0) Phillips band (red) for HD 22951 (top), HD 23016 (middle), and HD 23180 (bottom). The best-fit model parameters T_{kin}, n, and N are given in the legend. As in Fig. 1, the plots focus on segments around the C_2 transitions being considered for the fitting, and the wavelength grid is not continuous.

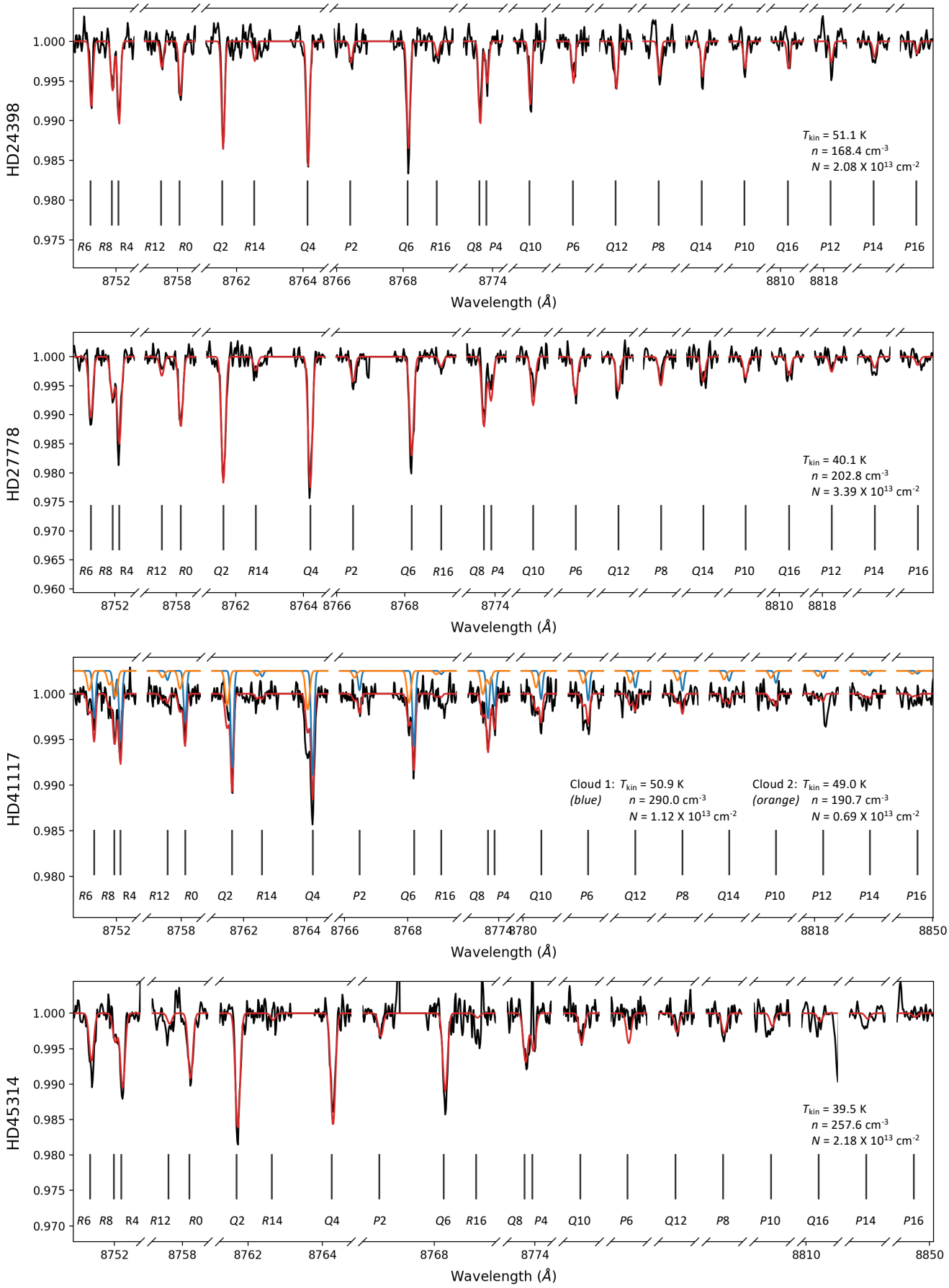

Fig. A.2. Same as Fig. A.1 but for HD 24398, HD 27778, HD 41117, and HD 45314. For HD 41117, synthetic spectra for individual velocity components are shown in orange and blue.

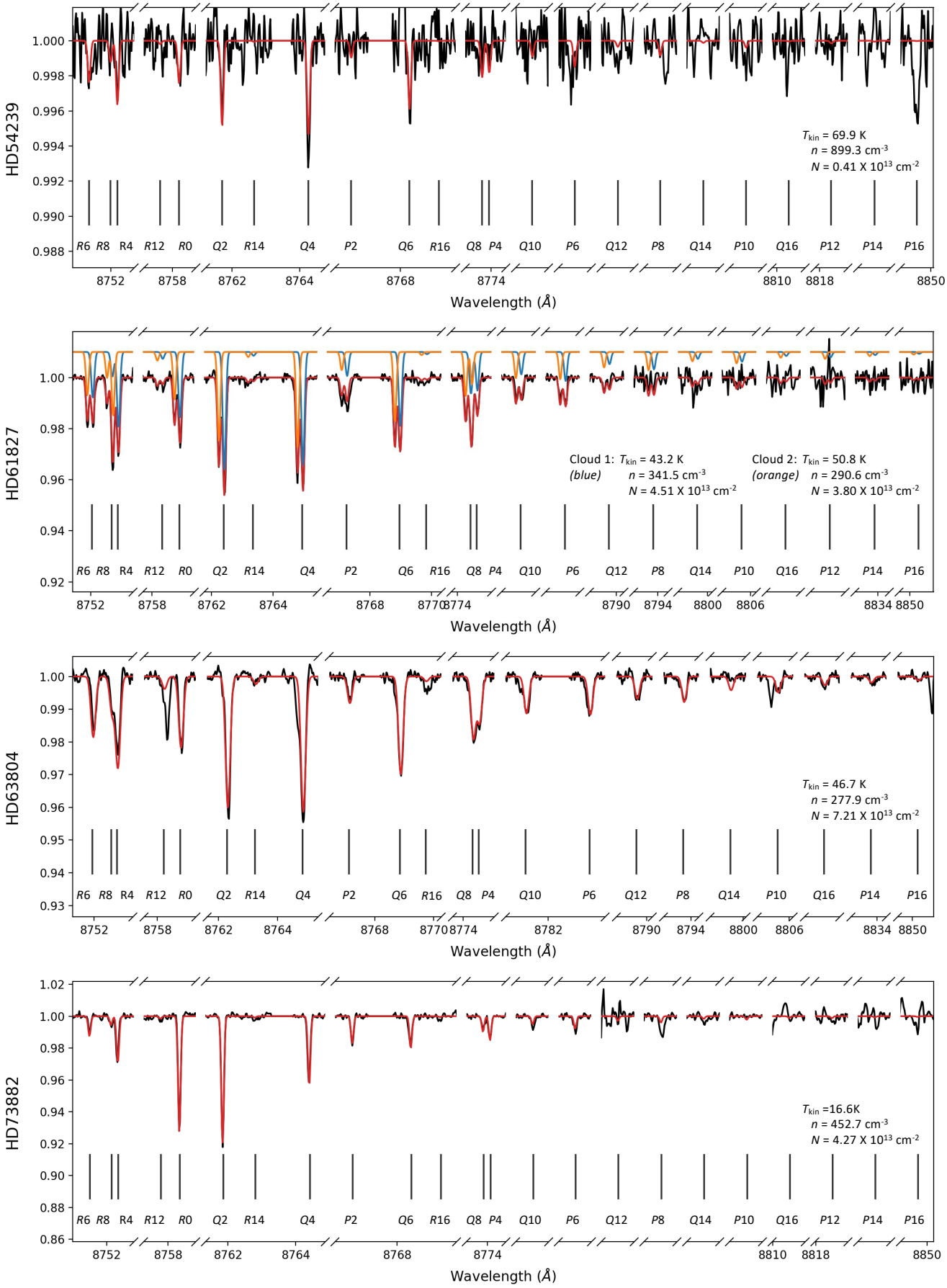

Fig. A.3. Same as Fig. A.1 but for HD 54239, HD 61827, HD 63804, and HD 73882. For HD 61827, synthetic spectra for individual velocity components are shown in orange and blue.

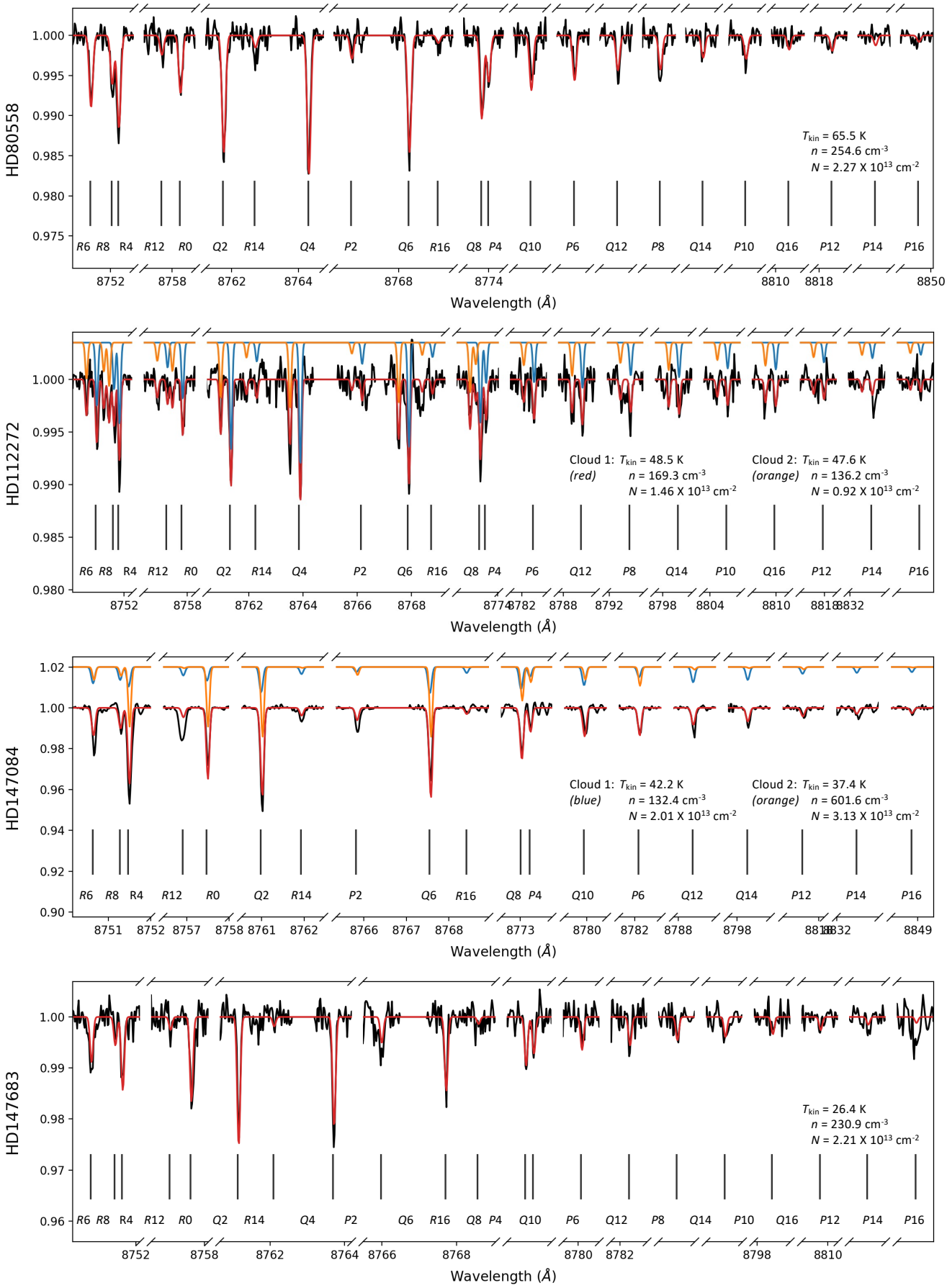

Fig. A.4. Same as Fig. A.1 but for HD 80558, HD 112272, HD 147084, and HD 147683. For HD 112272 and HD 147084, synthetic spectra for individual velocity components are shown in orange and blue.

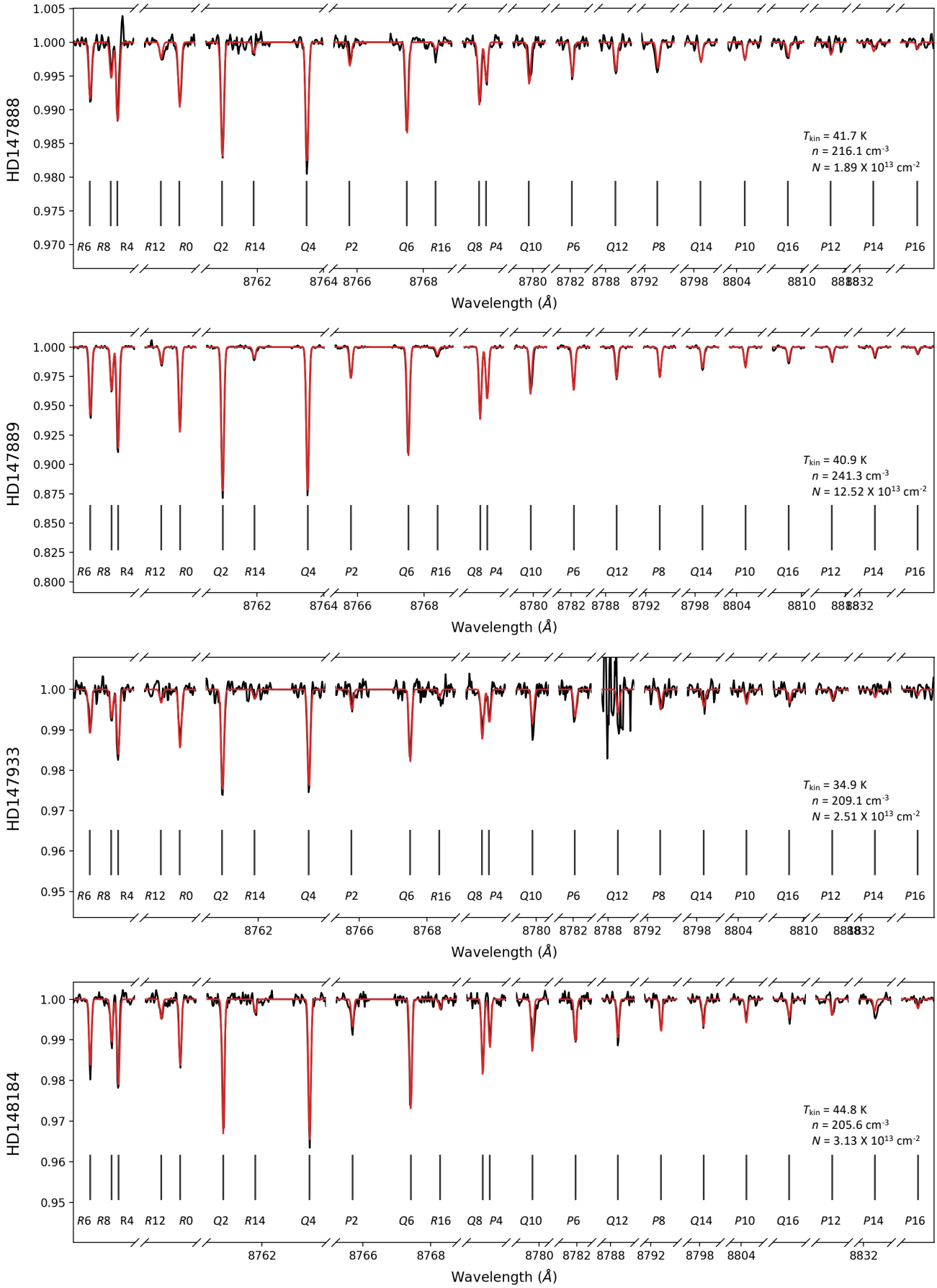

Fig. A.5. Same as Fig. A.1 but for HD 147888, HD 147889, HD 147933, and HD 148184.

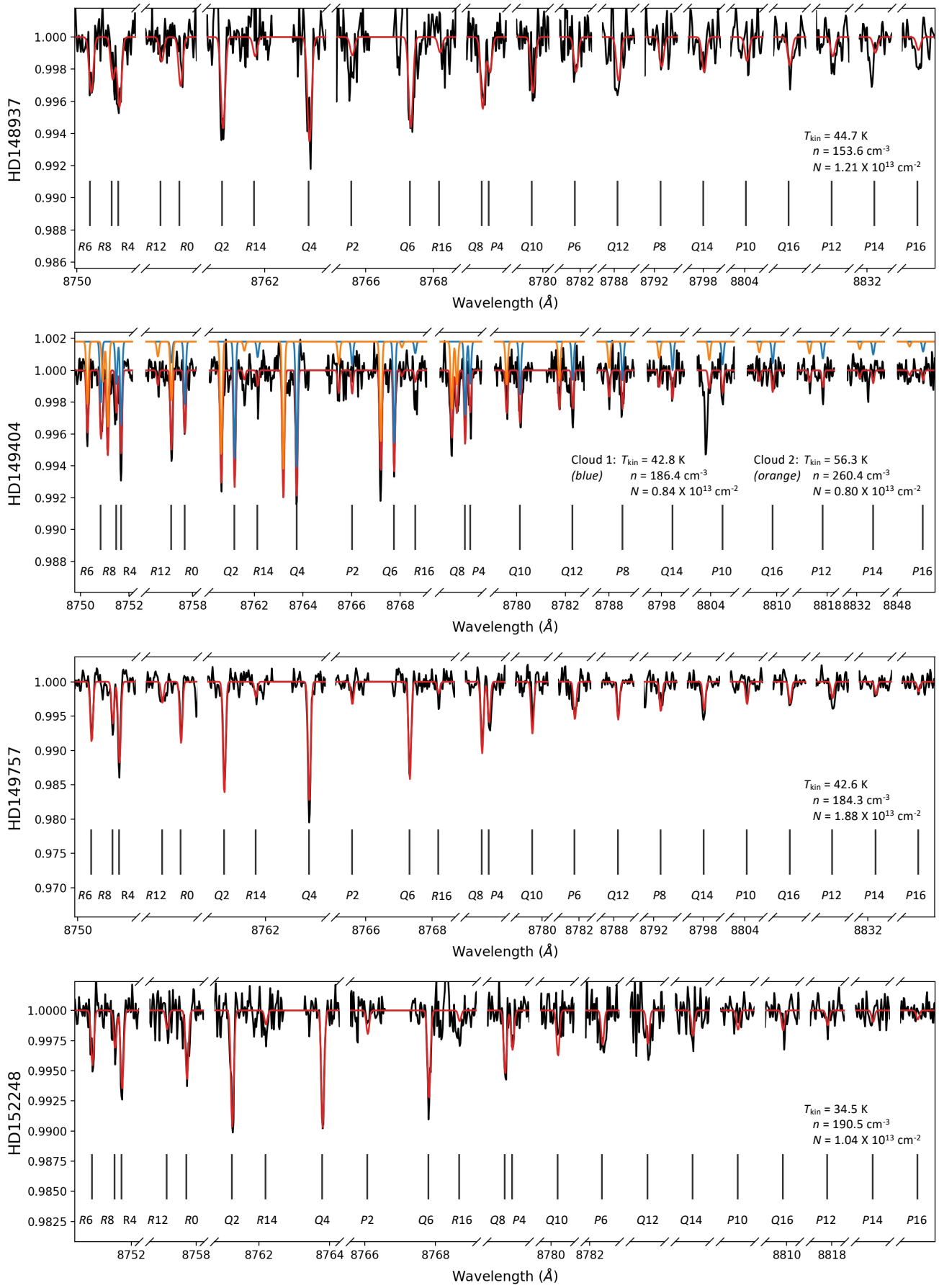

Fig. A.6. Same as Fig. A.1 but for HD 148937, HD 149404, HD 149757, and HD 152248. For HD 149404, synthetic spectra for individual velocity components are shown in orange and blue.

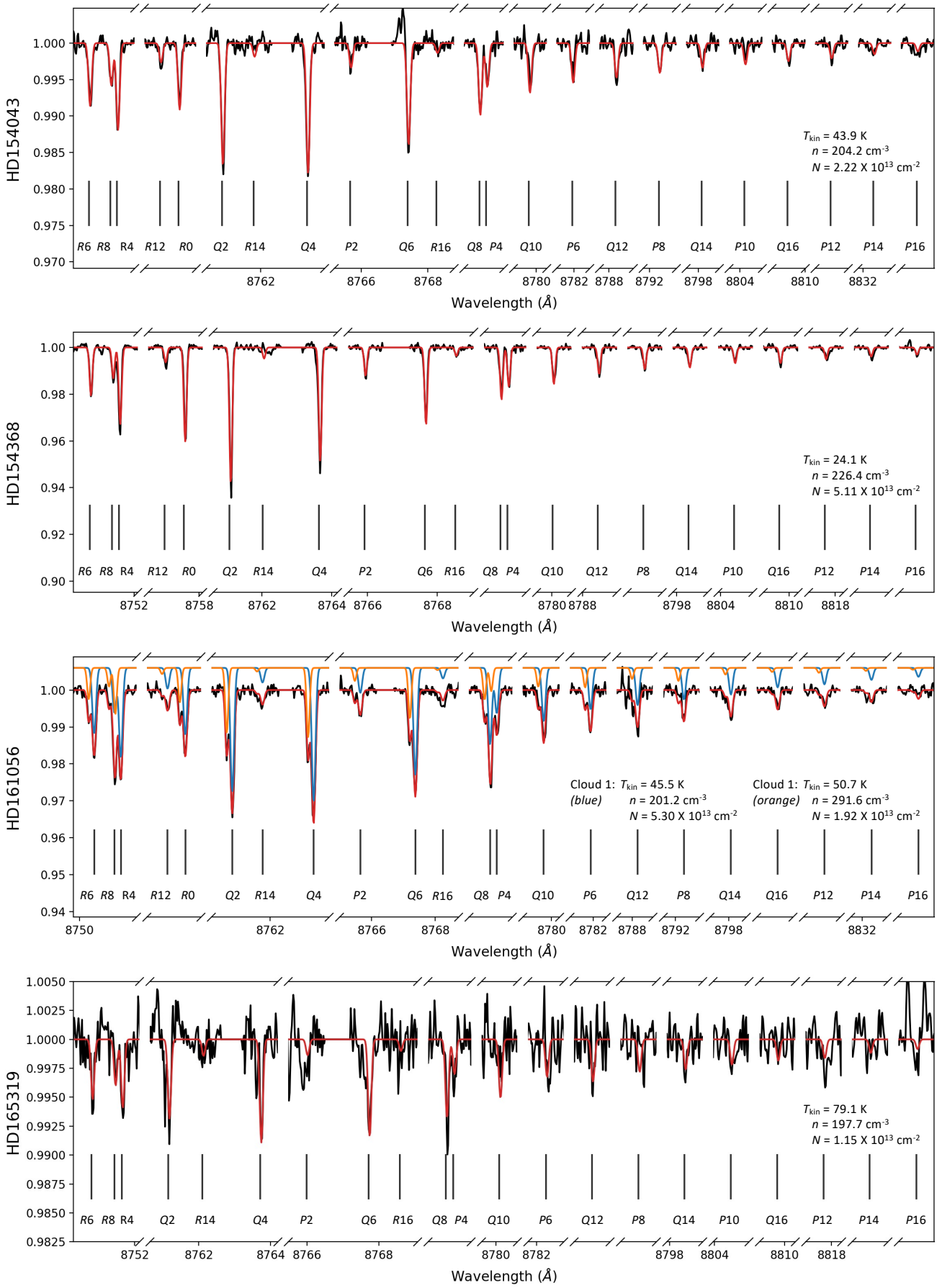

Fig. A.7. Same as Fig. A.1 but for HD 154043, HD 154368, HD 161056, and HD 165319. For HD 161056, synthetic spectra for individual velocity components are shown in orange and blue.

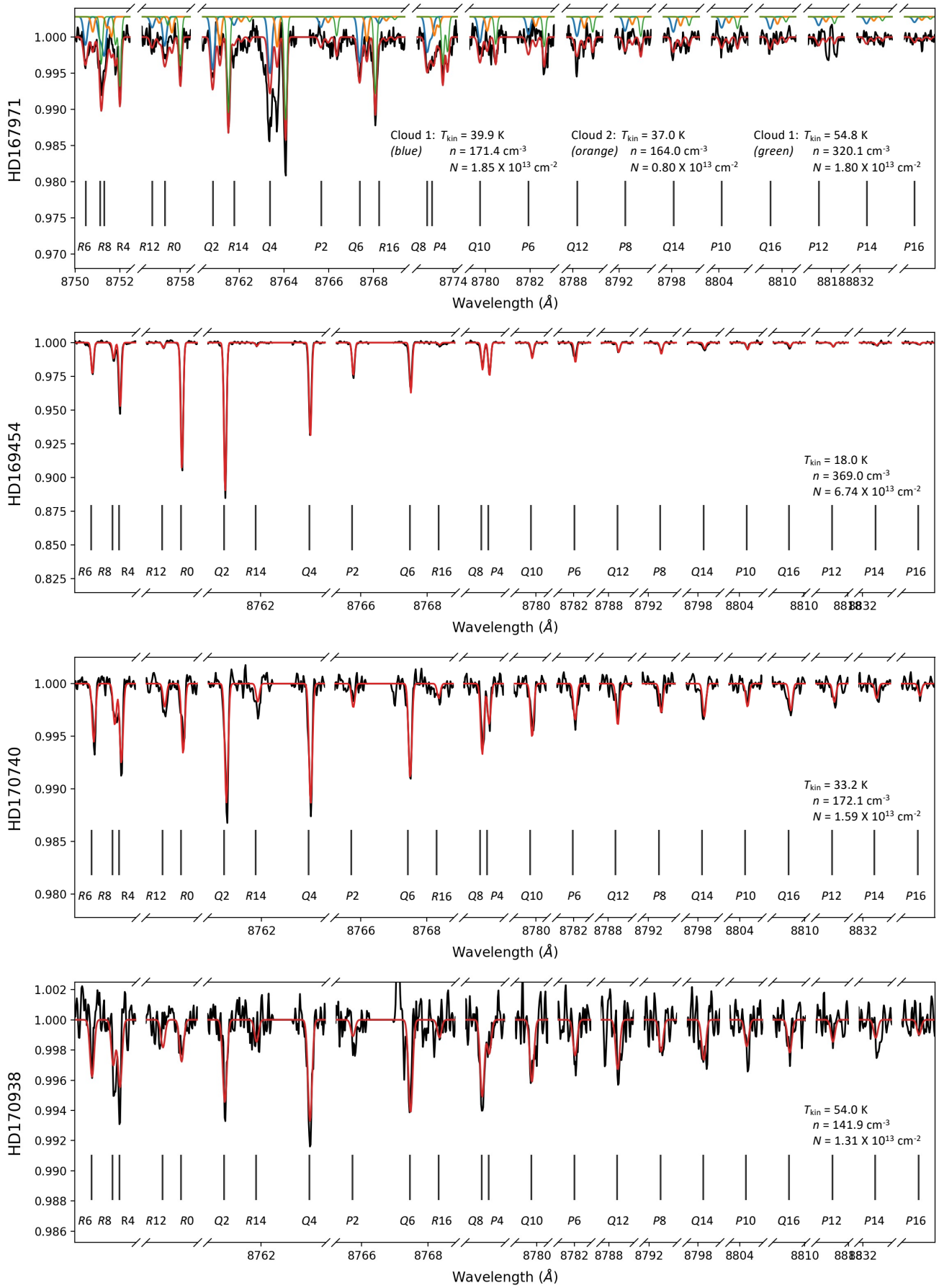

Fig. A.8. Same as Fig. A.1 but for HD 167971, HD 169454, HD 170740, and HD 170938. For HD 167971, synthetic spectra for individual velocity components are shown in orange, blue, and green.

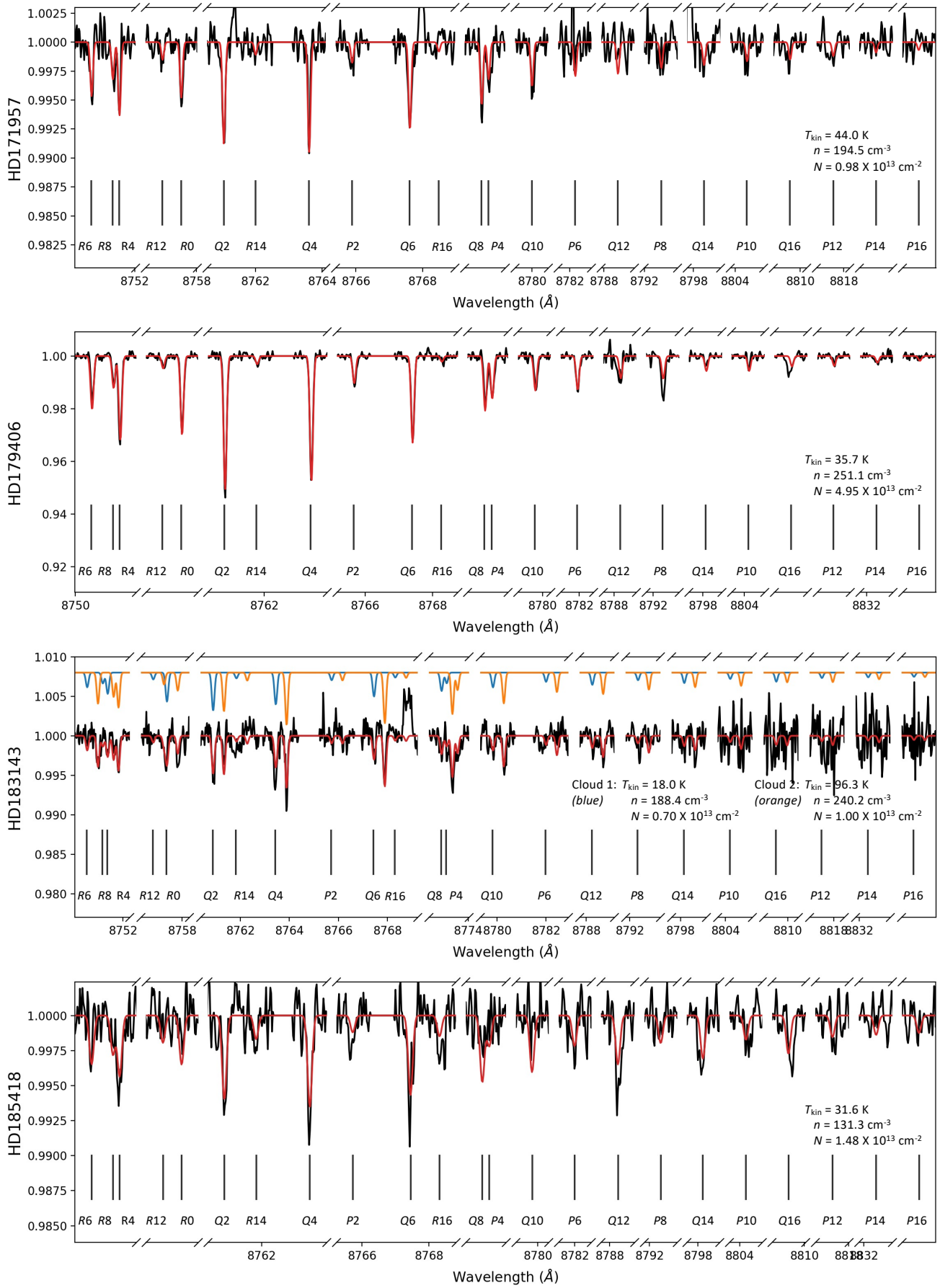

Fig. A.9. Same as Fig. A.1 but for HD 171957, HD 179406, HD 183143, and HD 185418. For HD 183143, synthetic spectra for individual velocity components are shown in orange and blue.

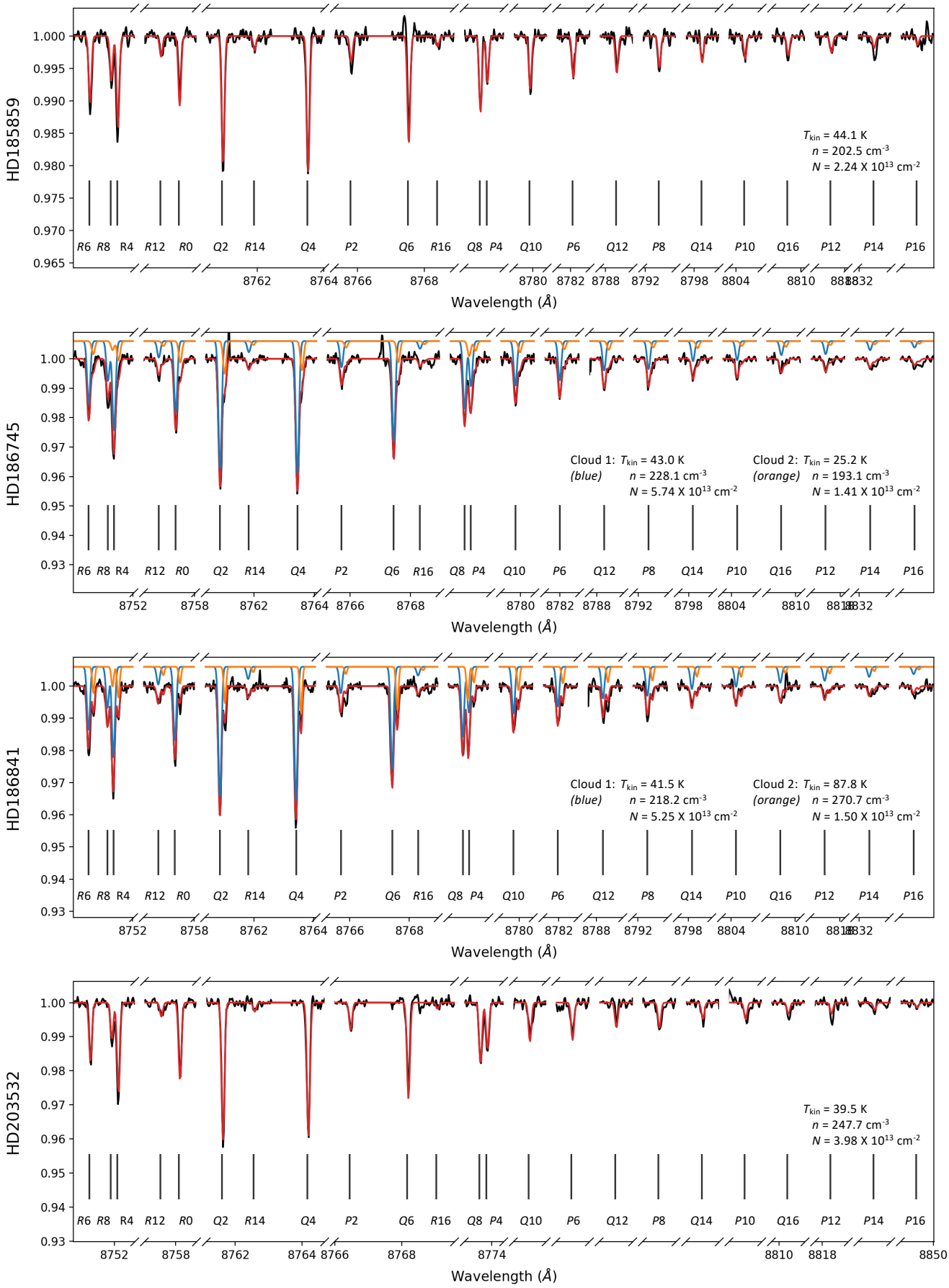

Fig. A.10. Same as Fig. A.1 but for HD 185859, HD 186745, HD 186841, and HD 203532. For HD 186745 and HD HD186841, synthetic spectra for individual velocity components are shown in orange and blue.

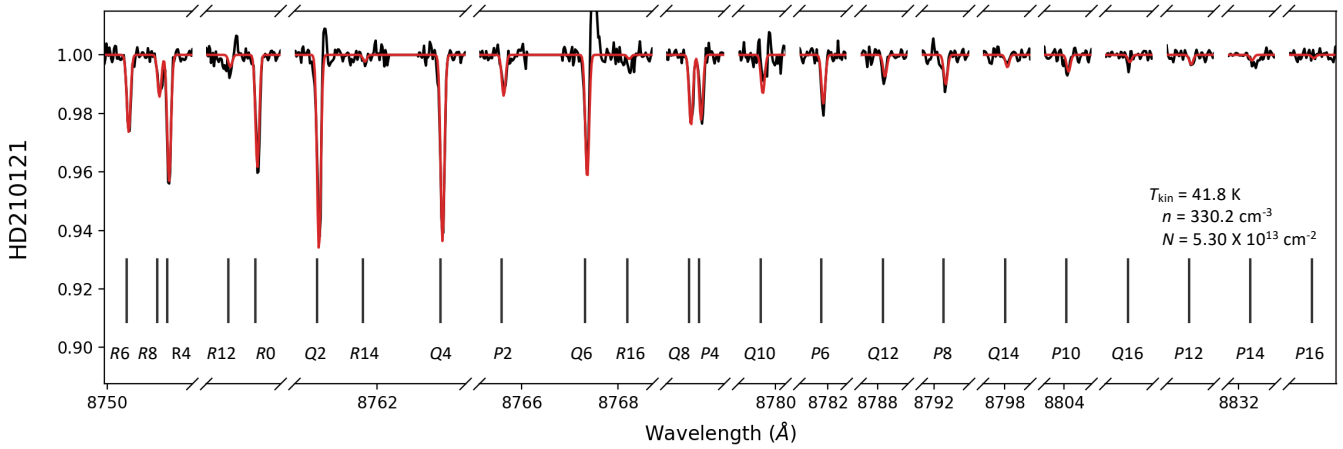

Fig. A.11. Same as Fig. A.1 but for HD 210121.

Appendix B: Fitted C_3 models

In this appendix we present plots of the best-fit model of the C_3 $\tilde{A} - \tilde{X}$ 000-000 electronic origin band compared to the normalised flux of the 27 sightlines where C_3 is detected or tentatively detected. Synthetic spectra for individual velocity components are plotted in different colours for the sightlines of HD 61827, HD 149404, HD 161056, and HD 186841. The excitation temperature of the lower $J \leq 14$ levels, $T_{\rm low}$, and the column density of C_3 N, are listed in the legend of each panel. We refer the reader to Sect. 4 for more details on the modelling process.

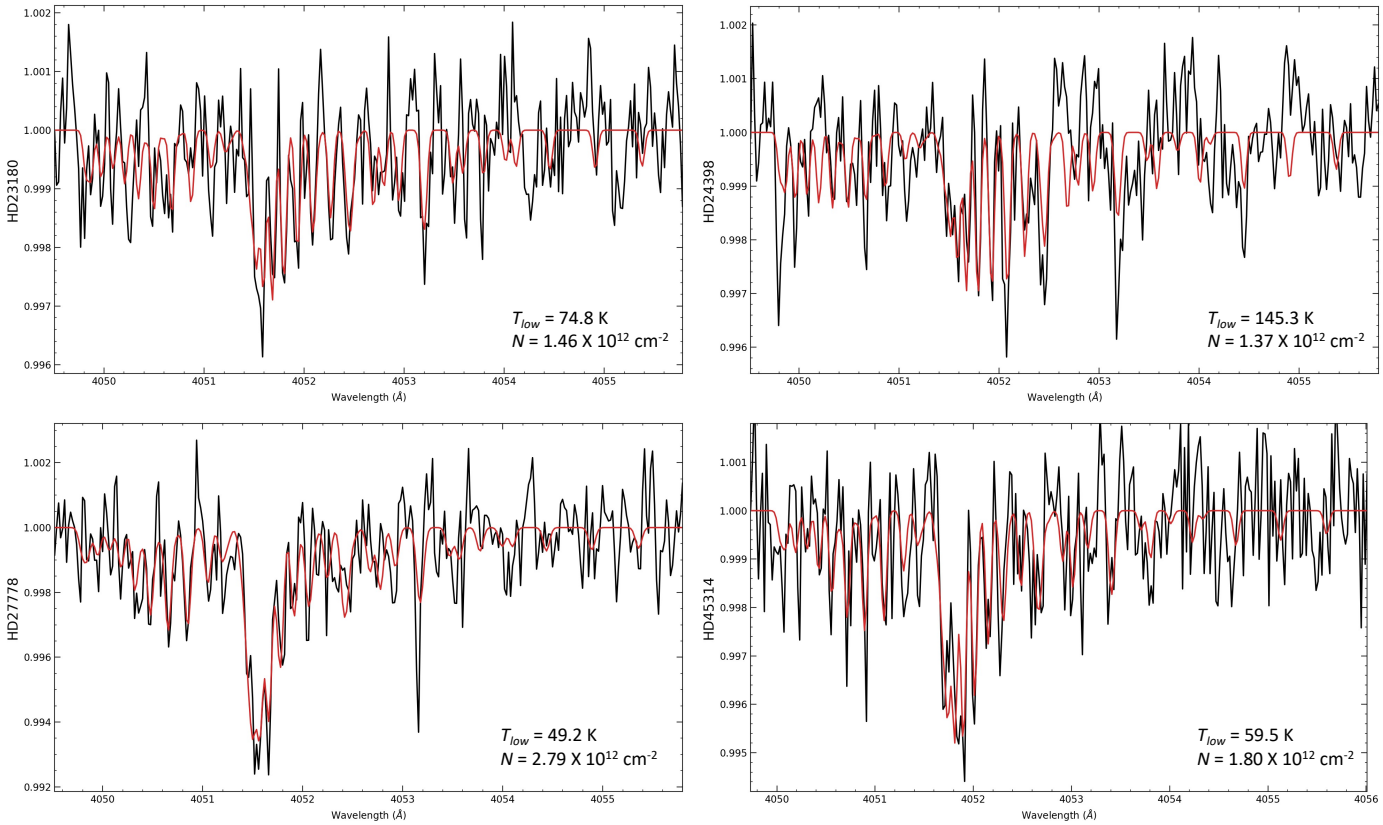

Fig. B.1. Normalised flux (black) and fitted model (red) of the C_3 $\tilde{A} - \tilde{X}$ 000-000 electronic origin band for HD 23180, HD 24398, HD 27778, and HD 45314. The model parameters $T_{\rm low}$ and N are listed in the legend of each panel.

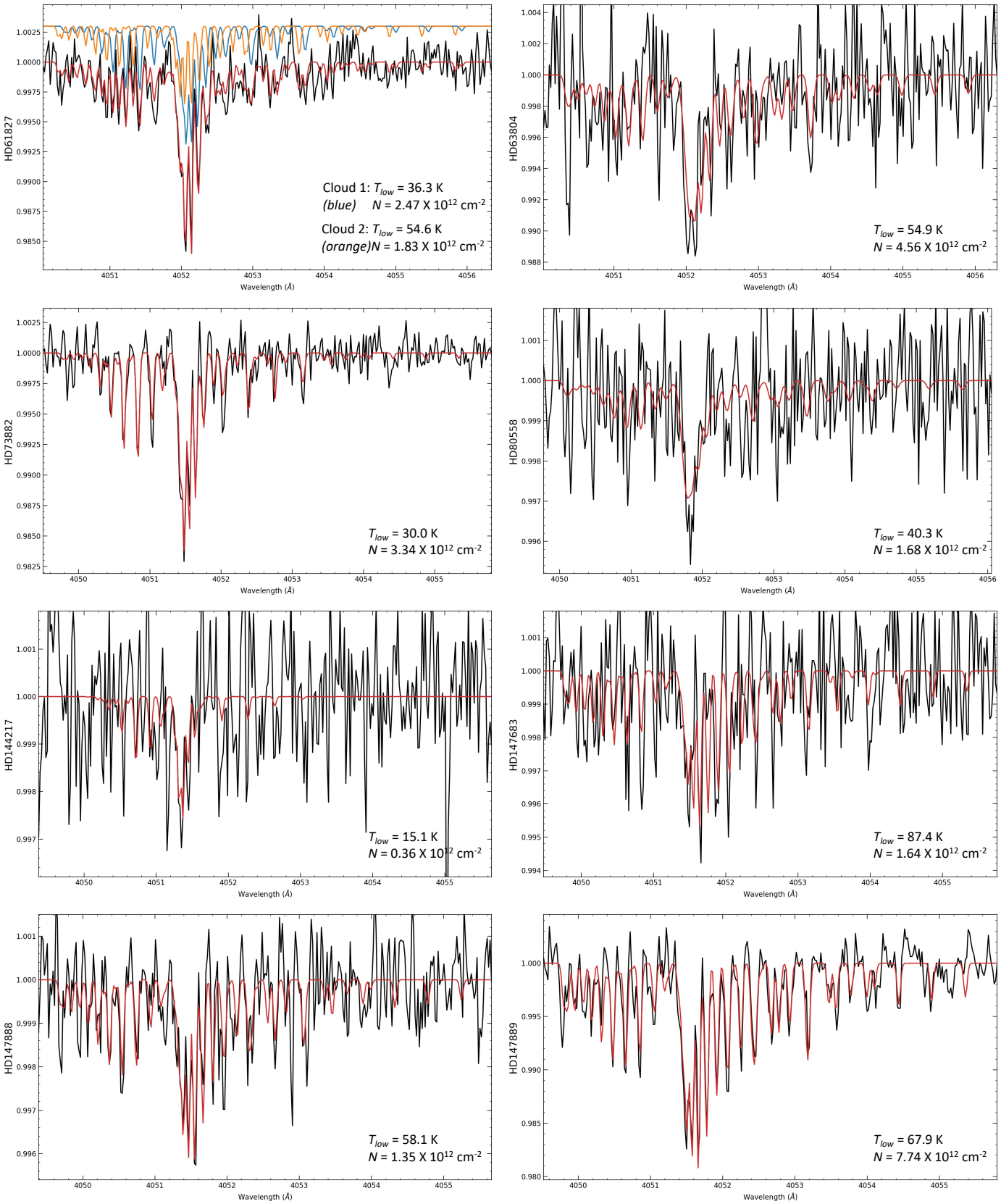

Fig. B.2. Same as Fig. B.1 but for HD 61827, HD 63804, HD 73882, HD 80558, HD 144217, HD 147683, HD 147888, and HD 147889. For HD 61827, synthetic spectra for individual velocity components are shown in orange and blue.

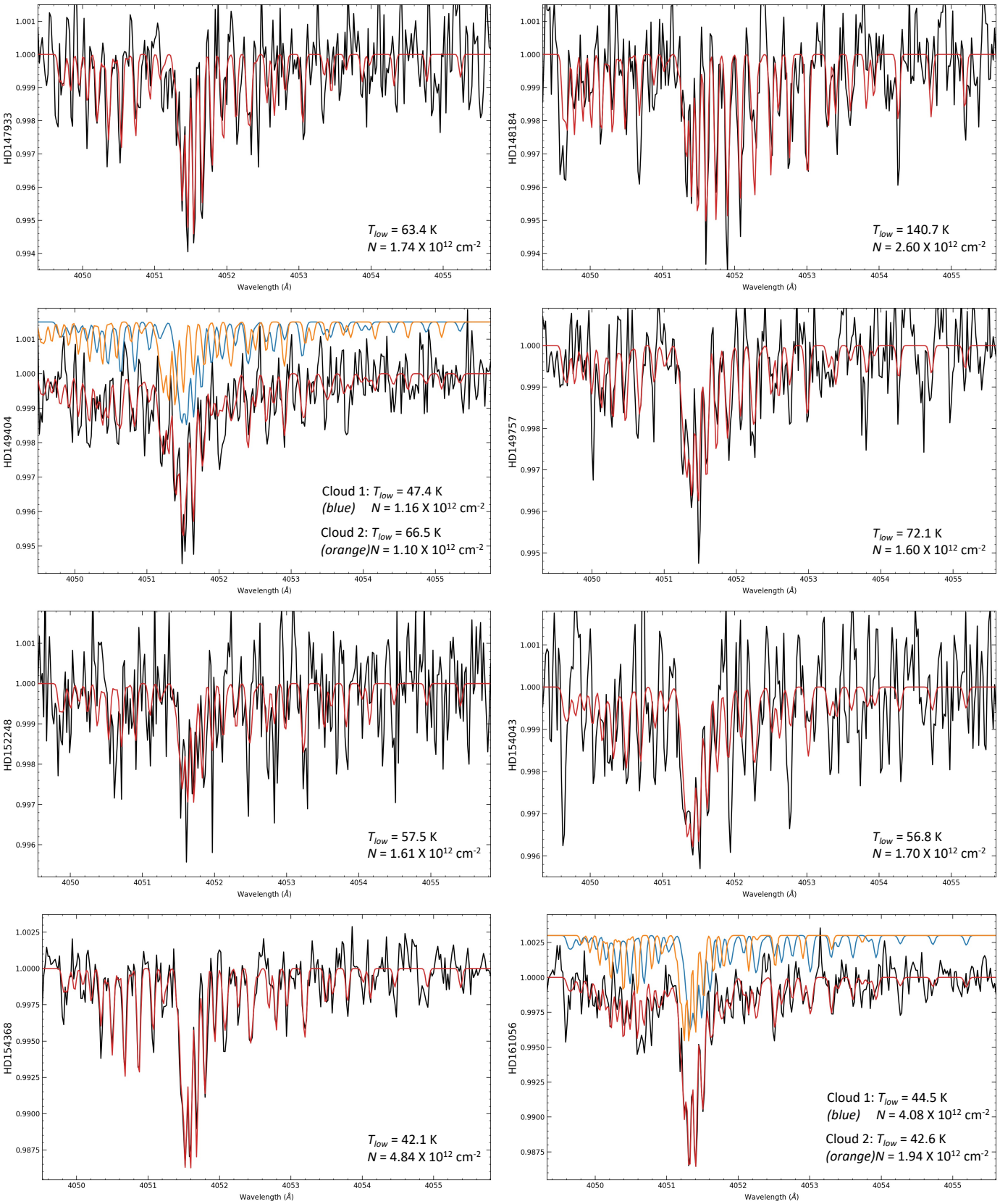

Fig. B.3. Same as Fig. B.1 but for HD 147933, HD 148184, HD 149404, HD 149757, HD 152248, HD 154043, HD 154368, and HD 161056. For HD 149404 and HD 161056, synthetic spectra for individual velocity components are shown in orange and blue.

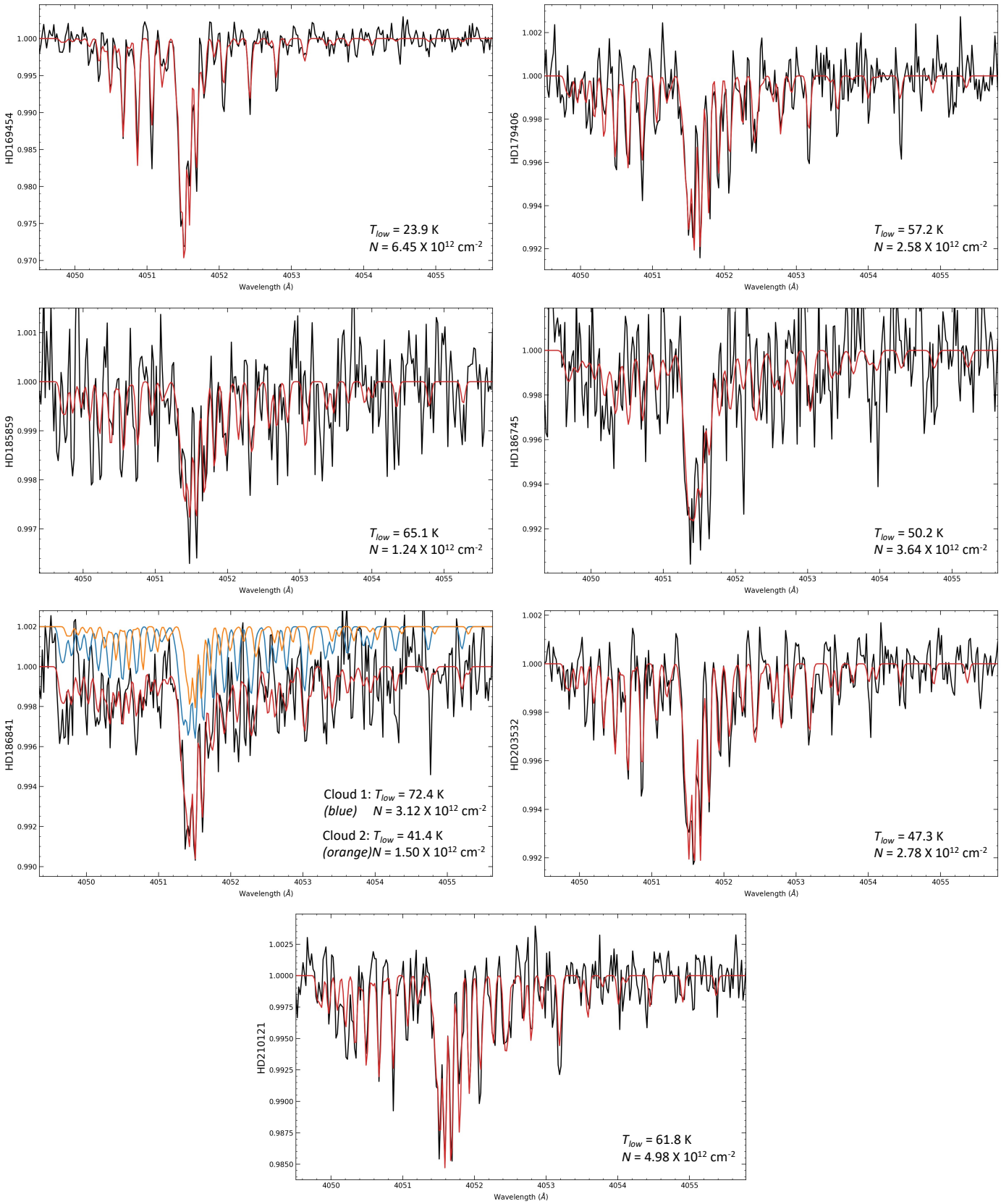

Fig. B.4. Same as Fig. B.1 but for HD 169454, HD 179406, HD 185859, HD 186745, HD 186841, HD 203532, and HD 210121. For HD 186841, synthetic spectra for individual velocity components are shown in orange and blue.

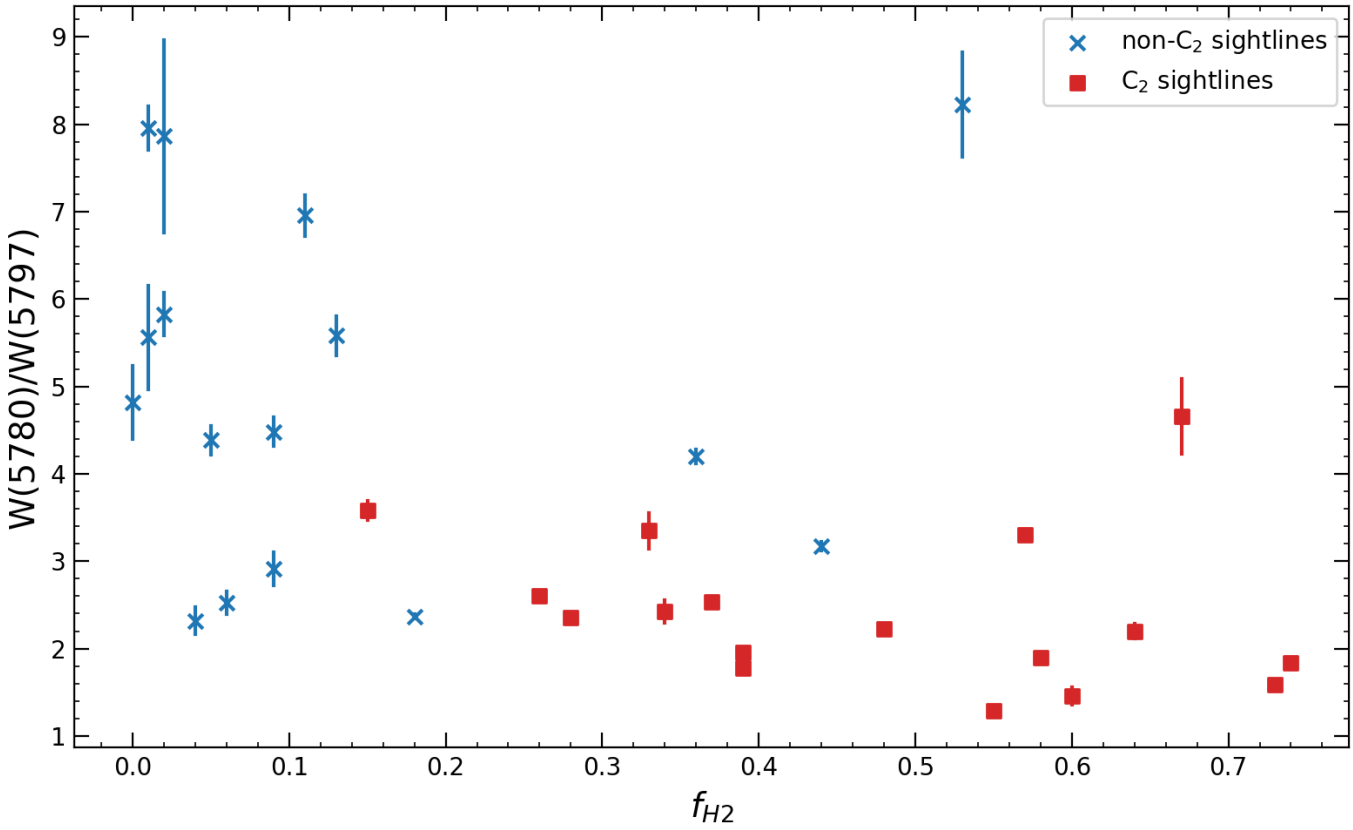

Fig. C.1. Behaviour of the $W(5780)/W(5797)$ ratio at different f_{H2} values. The DIB measurements are gathered from Fan et al. (2017). The sightlines with and without C_2/C_3 detections are highlighted in different colours. We find the C_2 sightlines are mostly ζ types that trace the denser interiors of the ISM clouds.

Appendix C: Physical conditions of C_2 sightlines

Figure C.1 compares the equivalent widths ratio between DIBs $\lambda\lambda$ 5780 and 5797 ($W(5780)/W(5797)$) among the C_2 and non-C_2 sightlines. The C_2 sightlines tend to have smaller $W(5780)/W(5797)$ ratios and large mass fraction of molecular hydrogen (f_{H2}), both of which are characteristic for ζ-type sightlines (e.g. Vos et al. 2011; Kos & Zwitter 2013).

Table C.1. Best-fit parameters of the C_2 model in our 40 sightlines, and literature values for comparison.

Sightline[a]	This Work					Literature		Ref
	T_{kin} (K)	n (cm^{-3})	N (10^{13} cm^{-2})	b ($km \cdot s^{-1}$)	v_{off}[b] ($km \cdot s^{-1}$)	T_{kin} (K)	n (cm^{-3})	
HD 22951[c]	$50.0^{+28.2}_{-5.4}$	$123.6^{+11.5}_{-10.3}$	$0.84^{+0.06}_{-0.06}$	$2.67^{+0.30}_{-0.27}$	$12.9^{+1.2}_{-1.2}$			
HD 23016[c]	$17.0^{+11.4}_{-2.0}$	$177.9^{+18.0}_{-11.6}$	$0.59^{+0.07}_{-0.04}$	$0.32^{+0.03}_{-0.04}$	$18.0^{+1.1}_{-1.1}$			
HD 23180	$37.7^{+2.3}_{-2.5}$	$193.1^{+4.4}_{-5.3}$	$2.49^{+0.04}_{-0.06}$	$2.37^{+0.12}_{-0.06}$	$13.3^{+1.1}_{-1.1}$	50	200^{+250}_{-50}	[1]
HD 24398	$51.1^{+5.8}_{-3.5}$	$168.4^{+5.8}_{-5.6}$	$2.08^{+0.05}_{-0.05}$	$1.53^{+0.08}_{-0.09}$	$13.9^{+1.1}_{-1.1}$	50	150^{+200}_{-50}	[1]
HD 27778	$40.1^{+1.9}_{-1.9}$	$202.8^{+5.2}_{-4.9}$	$3.39^{+0.05}_{-0.06}$	$2.40^{+0.07}_{-0.07}$	$15.3^{+1.1}_{-1.1}$	50±10	200^{+25}_{-25}	[1]
HD 41117	$50.9^{+1.0}_{-1.1}$	$290.0^{+7.6}_{-7.3}$	$1.12^{+0.03}_{-0.04}$	$1.45^{+0.11}_{-0.09}$	$15.1^{+1.1}_{-1.1}$			
	$49.0^{+19.4}_{-1.6}$	$190.7^{+33.9}_{-7.7}$	$0.69^{+0.04}_{-0.04}$	$2.56^{+0.22}_{-0.23}$	$9.7^{+1.2}_{-1.2}$			
HD 45314	$39.5^{+2.4}_{-2.4}$	$257.6^{+9.1}_{-9.5}$	$2.18^{+0.06}_{-0.05}$	$2.52^{+0.09}_{-0.10}$	$18.3^{+1.1}_{-1.1}$			
HD 54239[c]	$69.9^{+12.6}_{-8.1}$	$899.3^{+100.7}_{-448.8}$	$0.41^{+0.05}_{-0.04}$	$1.07^{+0.37}_{-0.49}$	$17.6^{+1.2}_{-1.2}$			
HD 61827	$43.2^{+1.0}_{-1.0}$	$341.5^{+9.1}_{-7.7}$	$4.51^{+0.05}_{-0.05}$	$1.73^{+0.04}_{-0.04}$	$41.8^{+1.0}_{-1.0}$			
	$50.8^{+0.6}_{-0.7}$	$290.6^{+4.6}_{-3.8}$	$3.80^{+0.05}_{-0.05}$	$1.53^{+0.05}_{-0.05}$	$35.8^{+1.0}_{-1.0}$			
HD 63804	$46.7^{+0.7}_{-0.7}$	$277.9^{+4.0}_{-4.3}$	$7.21^{+0.07}_{-0.06}$	$3.47^{+0.04}_{-0.05}$	$38.5^{+1.0}_{-1.0}$			
HD 73882	$16.6^{+0.3}_{-0.3}$	$452.7^{+8.4}_{-6.2}$	$4.27^{+0.03}_{-0.03}$	$0.75^{+0.04}_{-0.04}$	$22.1^{+1.0}_{-1.0}$	20±5	350^{+500}_{-150}	[1]
HD 80558	$65.5^{+3.0}_{-2.4}$	$254.6^{+9.5}_{-9.6}$	$2.27^{+0.04}_{-0.05}$	$2.05^{+0.08}_{-0.07}$	$19.5^{+1.1}_{-1.1}$			
HD 112272	$48.5^{+5.7}_{-3.2}$	$169.3^{+6.4}_{-6.4}$	$1.46^{+0.04}_{-0.04}$	$1.39^{+0.12}_{-0.11}$	$5.1^{+1.1}_{-1.1}$			
	$47.6^{+8.2}_{-9.1}$	$136.2^{+7.4}_{-8.8}$	$0.92^{+0.04}_{-0.05}$	$1.41^{+0.19}_{-0.17}$	$-9.8^{+1.1}_{-1.1}$			
HD 147084	$42.2^{+0.2}_{-12.3}$	$132.4^{+0.2}_{-72.9}$	$2.01^{+0.01}_{-0.85}$	$1.13^{+2.05}_{-0.01}$	$-7.1^{+1.3}_{-1.0}$	35±10	150^{+50}_{-25}	[2]

	$37.4^{+0.1}_{-9.0}$	$601.6^{+198.4}_{-82.2}$	$3.13^{+0.01}_{-0.43}$	$0.22^{+0.01}_{-0.03}$	$-6.0^{+1.0}_{-1.0}$			
HD 147683	$26.4^{+3.6}_{-2.1}$	$230.9^{+9.4}_{-8.6}$	$2.21^{+0.07}_{-0.07}$	$1.12^{+0.14}_{-0.15}$	$-1.1^{+1.1}_{-1.1}$	55±5	95	[3]
HD 147888	$41.7^{+1.6}_{-1.5}$	$216.1^{+4.4}_{-4.1}$	$1.89^{+0.03}_{-0.03}$	$1.30^{+0.05}_{-0.06}$	$-8.4^{+1.0}_{-1.0}$	55±5	200^{+50}_{-25}	[1]
HD 147889	$40.9^{+0.3}_{-0.4}$	$241.3^{+0.6}_{-1.6}$	$12.52^{+0.02}_{-0.08}$	$0.95^{+0.05}_{-0.01}$	$-7.8^{+1.0}_{-1.0}$	39±2	199±7	[4]
HD 147933	$34.9^{+1.5}_{-1.3}$	$209.1^{+3.9}_{-4.1}$	$2.51^{+0.04}_{-0.04}$	$1.12^{+0.07}_{-0.06}$	$-8.6^{+1.0}_{-1.0}$			[5]
HD 148184	$44.8^{+2.0}_{-2.3}$	$205.6^{+4.8}_{-4.4}$	$3.13^{+0.05}_{-0.05}$	$0.42^{+0.04}_{-0.03}$	$-11.7^{+1.0}_{-1.0}$	45±12	209±60	[4]
						50±15	150^{+100}_{-25}	[1]
HD 148937	$44.7^{+5.2}_{-10.1}$	$153.6^{+9.4}_{-9.0}$	$1.21^{+0.05}_{-0.06}$	$2.52^{+0.17}_{-0.15}$	$-14.6^{+1.1}_{-1.1}$			
HD 149404	$42.8^{+4.0}_{-3.4}$	$186.4^{+6.5}_{-7.8}$	$0.84^{+0.03}_{-0.04}$	$1.00^{+0.15}_{-0.13}$	$-0.1^{+1.1}_{-1.1}$			
	$56.3^{+4.8}_{-2.5}$	$260.4^{+21.2}_{-9.7}$	$0.80^{+0.03}_{-0.03}$	$1.31^{+0.12}_{-0.14}$	$-18.9^{+1.1}_{-1.1}$			
HD 149757	$42.6^{+1.1}_{-1.9}$	$184.3^{+4.3}_{-4.6}$	$1.88^{+0.04}_{-0.04}$	$0.99^{+0.09}_{-0.09}$	$-14.7^{+1.0}_{-1.0}$	43±19	177±55	[6]
						20±10	250^{+750}_{-50}	[7]
						30±10	250^{+250}_{-75}	[7]
						50± 5	150^{+25}_{-25}	[1]
HD 152248	$34.5^{+3.6}_{-3.4}$	$190.5^{+7.8}_{-6.6}$	$1.04^{+0.04}_{-0.03}$	$1.08^{+0.12}_{-0.14}$	$2.0^{+1.1}_{-1.1}$			
HD 154043	$43.9^{+1.4}_{-1.8}$	$204.2^{+4.5}_{-4.0}$	$2.22^{+0.04}_{-0.03}$	$1.75^{+0.05}_{-0.06}$	$-11.3^{+1.0}_{-1.0}$			
HD 154368	$24.1^{+0.6}_{-0.7}$	$226.4^{+2.0}_{-1.8}$	$5.11^{+0.04}_{-0.04}$	$0.97^{+0.04}_{-0.04}$	$-2.8^{+1.0}_{-1.0}$	30±2	204±8	[6]
						20±5	150^{+50}_{-25}	[1]
HD 161056	$45.5^{+0.8}_{-1.2}$	$201.2^{+2.1}_{-1.9}$	$5.30^{+0.04}_{-0.03}$	$2.24^{+0.03}_{-0.03}$	$-13.1^{+1.0}_{-1.0}$			
	$50.7^{+0.6}_{-0.8}$	$291.6^{+20.4}_{-3.8}$	$1.92^{+0.03}_{-0.03}$	$1.60^{+0.05}_{-0.06}$	$-19.0^{+1.0}_{-1.0}$			
HD 165319	$79.1^{+12.6}_{-5.5}$	$197.7^{+8.6}_{-26.8}$	$1.15^{+0.03}_{-0.10}$	$1.42^{+0.49}_{-0.09}$	$-1.5^{+1.1}_{-1.1}$			
HD 167971	$39.9^{+6.9}_{-1.0}$	$171.4^{+5.4}_{-4.5}$	$1.85^{+0.06}_{-0.07}$	$3.83^{+0.21}_{-0.17}$	$-12.9^{+1.2}_{-1.1}$			
	$37.0^{+20.3}_{-1.7}$	$164.0^{+11.4}_{-8.1}$	$0.80^{+0.06}_{-0.05}$	$2.84^{+0.33}_{-0.33}$	$-1.9^{+1.2}_{-1.2}$			[5]
	$54.8^{+1.0}_{-1.2}$	$320.1^{+21.2}_{-7.7}$	$1.80^{+0.05}_{-0.05}$	$2.35^{+0.12}_{-0.10}$	$11.1^{+1.1}_{-1.1}$			
HD 169454	$18.0^{+0.2}_{-0.2}$	$369.0^{+2.1}_{-2.1}$	$6.74^{+0.03}_{-0.03}$	$0.66^{+0.03}_{-0.03}$	$-8.7^{+1.0}_{-1.0}$	19±2	326±17	[4]
						20±5	200^{+50}_{-25}	[1]
						25	400±100	[8]
HD 170740	$33.2^{+2.8}_{-1.9}$	$172.1^{+4.3}_{-3.7}$	$1.59^{+0.04}_{-0.03}$	$1.76^{+0.06}_{-0.09}$	$-8.8^{+1.1}_{-1.1}$	21±9	161±16	[6]
HD 170938	$54.0^{+9.5}_{-4.3}$	$141.9^{+7.3}_{-5.2}$	$1.31^{+0.05}_{-0.05}$	$2.49^{+0.16}_{-0.16}$	$-9.3^{+1.1}_{-1.1}$			
HD 171957	$44.0^{+3.0}_{-6.3}$	$194.5^{+8.7}_{-8.7}$	$0.98^{+0.03}_{-0.04}$	$0.98^{+0.16}_{-0.15}$	$-4.7^{+1.1}_{-1.1}$			
HD 179406	$35.7^{+0.7}_{-0.8}$	$251.1^{+3.3}_{-3.3}$	$4.95^{+0.04}_{-0.05}$	$1.39^{+0.04}_{-0.04}$	$-12.0^{+1.0}_{-1.0}$	38±9	251±83	[4]
HD 183143	$18.0^{+13.5}_{-5.9}$	$188.4^{+20.3}_{-13.3}$	$0.70^{+0.19}_{-0.02}$	$2.13^{+0.12}_{-0.39}$	$-10.4^{+1.2}_{-1.3}$			[5]
	$96.3^{+3.8}_{-5.9}$	$240.2^{+28.5}_{-24.6}$	$1.00^{+0.06}_{-0.05}$	$1.98^{+0.21}_{-0.21}$	$4.7^{+1.1}_{-1.2}$			
HD 185418	$31.6^{+5.3}_{-4.8}$	$131.3^{+6.9}_{-6.0}$	$1.48^{+0.06}_{-0.06}$	$2.74^{+0.18}_{-0.18}$	$-10.6^{+1.1}_{-1.1}$			
HD 185859	$44.1^{+1.0}_{-0.9}$	$202.5^{+3.7}_{-3.2}$	$2.24^{+0.03}_{-0.03}$	$1.18^{+0.05}_{-0.05}$	$-7.5^{+1.0}_{-1.0}$			
HD 186745	$43.0^{+0.8}_{-0.9}$	$228.1^{+2.7}_{-2.8}$	$5.74^{+0.05}_{-0.05}$	$1.95^{+0.04}_{-0.03}$	$-10.6^{+1.0}_{-1.0}$			
	$25.2^{+3.6}_{-2.6}$	$193.1^{+7.2}_{-7.2}$	$1.41^{+0.05}_{-0.05}$	$1.89^{+0.12}_{-0.13}$	$-5.4^{+1.1}_{-1.1}$			
HD 186841	$41.5^{+1.0}_{-0.9}$	$218.2^{+2.5}_{-2.5}$	$5.25^{+0.05}_{-0.04}$	$1.84^{+0.04}_{-0.03}$	$-11.4^{+1.0}_{-1.0}$			
	$87.8^{+1.2}_{-13.1}$	$270.7^{+11.3}_{-10.3}$	$1.50^{+0.05}_{-0.03}$	$0.92^{+0.10}_{-0.14}$	$-5.6^{+1.1}_{-1.1}$			
HD 203532	$39.5^{+1.0}_{-1.7}$	$247.7^{+3.6}_{-4.5}$	$3.98^{+0.03}_{-0.05}$	$1.30^{+0.05}_{-0.03}$	$15.2^{+1.0}_{-1.0}$	30±10	210	[3]
HD 210121	$41.8^{+0.8}_{-0.9}$	$330.2^{+7.0}_{-6.7}$	$5.30^{+0.06}_{-0.06}$	$0.87^{+0.05}_{-0.06}$	$-13.7^{+1.0}_{-1.0}$	45±5	200^{+50}_{-50}	[1]
HD 23478						30± 10	190	[3]
HD 24534						45±10	200^{+50}_{-50}	[1]
HD 28975						30	125	[9]
HD 29647						10	≥ 175	[9]
						14±8	350^{+400}_{-150}	[10]
HD 62542						40±5	250^{+50}_{-25}	[11]
						30± 10	350^{+400}_{-100}	[1]
HD 76341						34±20	300±200	[4]
HD 80077						35	600±300	[8]
						20± 5	200^{+100}_{-25}	[1]
HD 114213						25	400±100	[8]
HD 115842						53±30	242±217	[6]
HD 136239						29±5	226±30	[6]
HD 148379						38±27	152±77	[6]
HD 151932						33±8	163± 20	[6]
HD 152236						27±7	176±24	[6]
HD 154445						18±18	101±17	[6]
HD 163800						38±15	169±43	[4]
HD 172028						30	300±100	[8]
						40±10	250^{+100}_{-50}	[1]
HD 177989						20	210	[3]

HD 198781		55±45	≤45	[3]
HD 200775		15±5	200^{+50}_{-25}	[1]
HD 204827		40±5	300^{+50}_{-50}	[1]
HD 206267		35±5	250^{+100}_{-25}	[1]
		30±10	280	[3]
HD 207198		60±10	200^{+25}_{-50}	[1]
HD 207308		35±15	190	[3]
HD 207538		35±15	150^{+25}_{-25}	[1]
HD 208266		10	210	[3]
HD 210839		30	100^{+50}_{-25}	[1]
HD 220057		90	165	[3]
BD+66° 1661		35±10	700±200	[12]
BD+66° 1674		60±10	800±400	[12]
BD+66° 1675		35±10	700±200	[12]
Cyg OB2 5		50	300±100	[13]
		35±15	150^{+50}_{-25}	[1]
Cyg OB2 12		35	300± 50	[13]
		40±15	200^{+75}_{-50}	[1]
Cyg OB2 12, Comp. 2		30±5	100±7	[14]
Cyg OB2 12, Comp. 3		25±5	125±7	[14]
SN2008fp		30	250	[15]
Cernis 52		40±10	250±50	[16]
Sk 143		25	600	[17]

References. [1] Sonnentrucker et al. (2007); [2] van Dishoeck & Black (1989); [3] Hupe et al. (2012); [4] Kaźmierczak et al. (2010a); [5] Thorburn et al. (2003); [6] Kaźmierczak et al. (2010b); [7] Crawford (1997) [8] Gredel (1999); [9] Federman et al. (2021); [10] Hobbs et al. (1983); [11] Welty et al. (2020); [12] Gredel (2004); [13] Gredel et al. (2001); [14] Hamano et al. (2019); [15] Cox & Patat (2014); [16] Iglesias-Groth (2011); [17] Welty et al. (2013)

Notes. The last part of the table (below the line) contains literature values only, and only for sightlines for which both $T_{\rm kin}$ and n are determined. [(a)]For sightlines that harbour multiple velocity components, the best-fit results are listed for each component in separate entries. [(b)]Relative to the barycentric frame.
[(c)]Tentative detection where no individual transition reached the 3σ detection limit.